

A New Context-Aware Details Injection Fidelity With Adaptive Coefficients Estimation for Variational Pansharpening

Jin-Liang Xiao[✉], Ting-Zhu Huang[✉], Member, IEEE, Liang-Jian Deng[✉], Member, IEEE,
Zhong-Cheng Wu[✉], and Gemine Vivone[✉], Senior Member, IEEE

Abstract—Pansharpening is related to the fusion of a low spatial resolution multispectral (MS) image retaining an abundant spectral content and a high spatial resolution panchromatic (PAN) image to obtain a product with both the abundant spectral content of the former and the high spatial resolution of the latter. Many previous studies are only focused on the global or local relationship between the PAN image and the corresponding high-resolution multispectral (HRMS) image. However, we found that the relationship between PAN and HRMS images in the gradient domain can be better explored through the image context. In this article, we propose context-aware details injection fidelity (CDIF) with adaptive coefficients estimation, which can fully explore the complicated relationship between the PAN image and the HRMS image in the gradient domain. More specifically, we apply a clustering method to divide the pixels of an image into different context-based regions. Afterward, the adaptive coefficients are estimated by using a regression-based method for each region. The CDIF is effective in extracting the main features from the two inputs to be fused. In addition, we integrate the CDIF with a conventional fidelity term and a total variation regularization to formulate a novel variational pansharpening model that is solved by designing an algorithm based on the alternating direction method of multiplier (ADMM) framework. Qualitative and quantitative assessments on different datasets support the effectiveness and robustness of the proposed method. The code is available at <https://github.com/liangjiandeng/CDIF>.

Index Terms—Adaptive coefficients, context-aware fidelity, image fusion, pansharpening, remote sensing, variational models.

NOMENCLATURE

\mathcal{X} , \mathbf{X} , \mathbf{x} , and x	Tensor, matrix, vector, and scalar.
$\mathcal{X} \in \mathbb{R}^{H \times W \times S}$	HRMS image.
$\mathbf{X} \in \mathbb{R}^{S \times HW}$	Mode-3 unfolding of \mathcal{X} .
$\mathcal{X}_i \in \mathbb{R}^{H \times W}$	i th band of the HRMS image \mathcal{X} .
$\mathcal{Y} \in \mathbb{R}^{h \times w \times S}$	MS image.

Manuscript received November 23, 2021; revised January 7, 2022 and February 1, 2022; accepted February 20, 2022. Date of publication February 24, 2022; date of current version April 5, 2022. This work was supported in part by the National Natural Science Foundation of China under Grant 12171072 and Grant 61702083, in part by the Key Projects of Applied Basic Research in Sichuan Province under Grant 2020YJ0216, and in part by the National Key Research and Development Program of China under Grant 2020YFA0714001. (Corresponding authors: Ting-Zhu Huang; Liang-Jian Deng.)

Jin-Liang Xiao, Ting-Zhu Huang, Liang-Jian Deng, and Zhong-Cheng Wu are with the School of Mathematical Sciences, University of Electronic Science and Technology of China, Chengdu, Sichuan 611731, China (e-mail: jinliang_xiao@163.com; tingzhuhuang@126.com; liangjian.deng@uestc.edu.cn; wuzhch97@163.com).

Gemine Vivone is with the National Research Council—Institute of Methodologies for Environmental Analysis (CNR-IMAA), 85050 Tito, Italy (e-mail: gemine.vivone@imaa.cnr.it).

Digital Object Identifier 10.1109/TGRS.2022.3154480

$\mathbf{Y} \in \mathbb{R}^{S \times hw}$	Mode-3 unfolding of the MS image \mathcal{Y} .
$\mathbf{P} \in \mathbb{R}^{H \times W}$	PAN image.
$\mathcal{P} \in \mathbb{R}^{H \times W \times S}$	Extended PAN image, \mathbf{P} , with S bands.
$\overline{\mathbf{P}} \in \mathbb{R}^{S \times HW}$	Mode-3 unfolding of the extended PAN image.
$\mathbf{G} \in \mathbb{R}^{S \times 2HW}$	Adaptive coefficient.
\circ	Hadamard product.
\oslash	Elementwise division.
$\nabla_i, i = 1, 2, 3$	Gradient operation along the i th direction.
$\nabla = \begin{bmatrix} \nabla_1 \\ \nabla_2 \end{bmatrix}$	Gradient operation along the spatial directions.
$\nabla \mathcal{X} \in \mathbb{R}^{2H \times W \times S}$	\mathcal{X} in the gradient domain.
$\nabla \mathbf{X} \in \mathbb{R}^{S \times 2HW}$	Mode-3 unfolding of $\nabla \mathcal{X}$.

I. INTRODUCTION

REMOTE sensing has several applications, such as detection, analysis, and forecasting. Satellites, e.g., IKONOS, QuickBird, WorldView-2, Pléiades, and WorldView-3, acquire more information. However, because of hardware limitations, we can design acquisition sensors with only one high resolution, usually penalizing the others. Thus, high spatial resolution panchromatic (PAN) images can be acquired together with data showing a greater focus on the spectral resolution as low spatial resolution multispectral (MS) images [1]. The goal of pansharpening (which stands for PAN sharpening) is to fuse the abovementioned pairs to obtain high-resolution multispectral (HRMS) images.

A. Related Works

Pansharpening methods can be roughly divided into four classes [2]–[4], i.e., component substitution (CS) methods, multiresolution analysis (MRA) approaches, machine learning (ML) techniques, and variational optimization (VO)-based methods. More details about the abovementioned categories can be found in [1].

The CS methods, commonly considered classic approaches for pansharpening, are based on the substitution of one or more components after applying a reversible spectral transformation. This latter is applied to the MS image with the aim of separating the spatial and spectral information. The spatial

information is substituted with the PAN image to enhance the spatial resolution of the MS image. Some instances of these approaches are the Brovey transform [5], the principal component analysis (PCA) [6], the intensity–hue–saturation (IHS) [7], the Gram–Schmidt (GS) spectral sharpening [8], the partial replacement adaptive CS (PRACS) [9], and the band-dependent spatial detail (BDSD) [10] methods. For these techniques, the tradeoff between spatial and spectral distortions is impossible to be overcome. Thus, CS methods have a good spatial fidelity but paying it with a greater spectral distortion.

The MRA methods rely upon the injection of spatial details extracted from the PAN image into the MS image. Unlike CS methods, they can preserve spectral information but causing (usually evident) spatial distortions. Spatial details can be extracted from different decomposition methods. Some instances of approaches in the MRA class are the smoothing filter-based intensity modulation (SFIM) [11], the decimated wavelet transform (DWT) [12], the undecimated wavelet transform (UDWT) [13], the “ α -trous” wavelet transform (ATWT) [14], the generalized Laplacian pyramid (GLP) [15], and some methods, i.e., [16] and [17], which propose strategies to extract details in an accurate way.

ML approaches have recently achieved great success in several image processing fields, including pansharpening [18]–[25]. Many ML methods for pansharpening, e.g., [26]–[30], have a strong ability in feature extraction. Hence, the relationship among MS, PAN, and HRMS images can be well-expressed by these methodologies. However, the other side of the coin is represented by: 1) the need for training data and computing resources; 2) a lack of robustness with respect to the changes of acquisition sensors and scenarios under analysis; and 3) the assumption usually made by these methods imposing that the relationship among MS, PAN, and HRMS images learned at reduced resolution is the same as that of at full resolution. Thus, the effectiveness of these approaches in addressing operative scenarios is often compromised. Besides, some advanced ML techniques, e.g., the graph convolutional network (GCN) [31] and SpectralFormer [32], showed their potentialities in hyperspectral image processing [33]. These techniques can effectively extract feature information. However, their validity for the pansharpening problem needs to be explored and verified.

In recent years, VO methods have become more popular due to their flexibility [34]. They can show a good ability in modeling the relationship among MS, PAN, and HRMS images. Ballester *et al.* [35] assumed that the PAN image is a linear combination of the different bands of the HRMS image, thus proposing the P+XS model. In this category, we can express the connections among MS, PAN, and HRMS in several domains. For example, Deng *et al.* [36] built the model based on reproducible kernels in the Hilbert space, Fu *et al.* [37] proposed a VO model based on a local gradient constraint (LGC), and Zhuang *et al.* [38] used gradient domain guided image filtering for both preserving image structures and suppressing artifacts and noise. Moreover, the use of different norms is sometimes considered. For instance, Deng *et al.* [39] proposed a pansharpening model with a hyper-Laplacian prior using an ℓ_p ($0 < p < 1$) norm to describe the relationship

between the HRMS image and the upsampled MS image in the gradient domain [40]; instead, Wu *et al.* [41] applied an $\ell_{2,1}$ norm to constrain the HRMS image and the PAN image in the gradient domain, again. VO methods can improve spatial information of the original MS image without affecting the spectral content by solving optimization problems. However, the definition of appropriated fidelity terms is a hard task, resulting in a reduction of the performance when this operation is not properly performed.

B. Contributions

A context-aware details injection fidelity (CDIF) with adaptive coefficients estimation is proposed in this article to obtain spatial structure features from the PAN image. The CDIF describes the relationship between PAN and HRMS images in the gradient domain. Unlike local and global approaches, we explore the relationship based on the image context. This latter can be drawn in an accurate way (please see Section V-E3 for more details). The PAN image retains more spatial information than the original MS image. Thus, the CDIF can obtain this spatial information from the PAN image due to the exploitation of a context-based approach.

On the above basis, we integrate the proposed CDIF with two conventional fidelity and regularization terms to formulate a novel variational pansharpening model. The framework of the proposed model is shown in Fig. 1. Moreover, we design an algorithm that is based on the alternating direction method of multiplier (ADMM) [42] framework to effectively solve the proposed model. In our experiments, we compare this approach with some state-of-the-art methods on data acquired by different satellites, e.g., IKONOS, QuickBird, Pléiades, WorldView-2, and WorldView-3. The proposed model has shown good performance when applied to different satellite data getting remarkable robustness.

The *contributions* of this article are summarized as follows.

- 1) We propose a CDIF that can draw the context-aware relationship between PAN and HRMS images with adaptive coefficients estimation.
- 2) A variational model, including the proposed CDIF and two conventional fidelity and regularization terms, is formulated for the task of remote sensing pansharpening. Moreover, an ADMM-based algorithm is designed to effectively solve the proposed model.
- 3) Extensive experiments on several reduced and full-resolution datasets demonstrate the superiority of the proposed approach compared with recent state-of-the-art pansharpening techniques.

C. Organization

The rest of this article is organized as follows. Section II briefly introduces the notation and the motivations behind this work. In Section III, we give an interpretation of the proposed model. The algorithm designed to solve the proposed model is described in Section IV. Instead, Section V is devoted to the experimental results with a particular emphasis on analyzing the parameters and discussing some details about the proposed method. Finally, concluding remarks are drawn in Section VI.

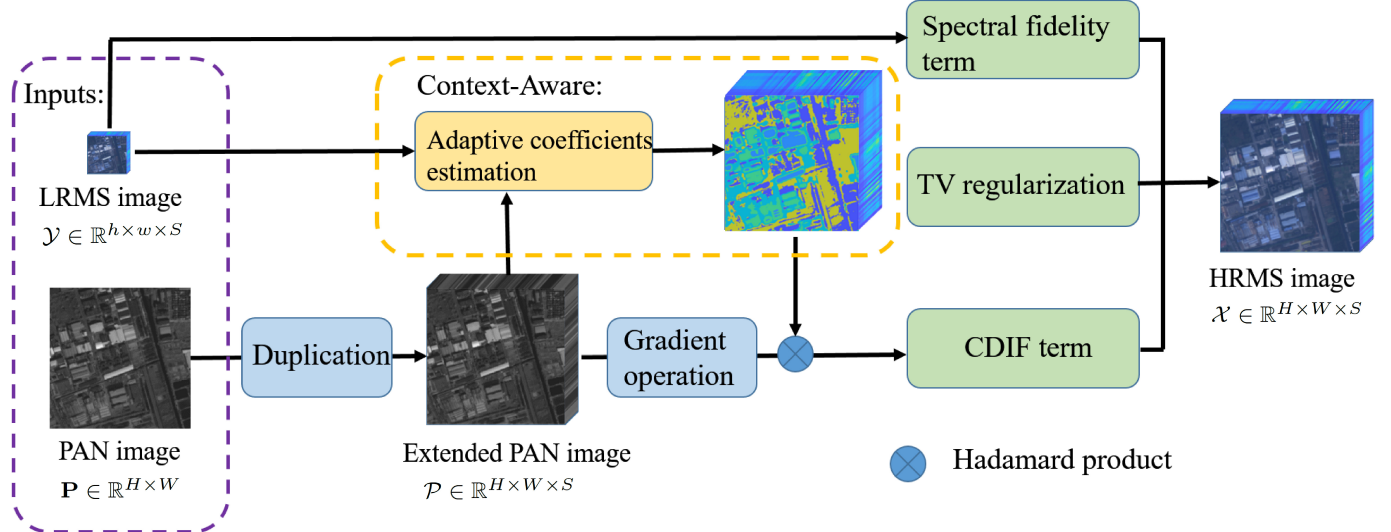


Fig. 1. Framework of our model. The details of our framework can be found in Section III.

II. NOTATION AND MOTIVATIONS

The notation is summarized in the Nomenclature. Instead, the motivations behind this work are introduced in the following.

A. Motivations

A widely used assumption performed in the literature is that the PAN image and the HRMS image share common spatial structures. Starting from this consideration, spatial structures are extracted from the PAN image using several methodologies. Many previous works consider the relationship between the PAN and the HRMS images in a direct way. For instance, the P+XS method [35] assumes that the PAN image is the weighted sum of the HRMS bands. However, this direct approach can lead to a reduction of the overall accuracy of the approach. Thus, we propose to extract the spatial information from the PAN image but working in the gradient domain. Information in the gradient domain has demonstrated its usefulness for low-level vision tasks, including pansharpening, since it can describe, in a better way, dominant image structures to represent crucial image features. As shown in Fig. 2, it is evident that the PAN image approximates, in a better way, the HRMS bands in the gradient domain with respect to the original intensity domain. Hence, we can obtain spatial features in an easier way working in the gradient domain than the original one. This cue motivates us to explore the relationship between PAN and HRMS images in the gradient domain, unlike what is usually proposed in the literature.

Many previous methods are focused on the global or local relationship between the PAN image and the HRMS image. For instance, Wu *et al.* [41] consider a global relationship; instead, Fu *et al.* [37] investigate on a local linear relationship among image patches. However, global and local relationships are not generally enough to accurately describe the complex relationship between the two input data [see Fig. 2(b)], where the relationship between each band of the HRMS image and the PAN image is pixel-dependent. Thus, in this article,

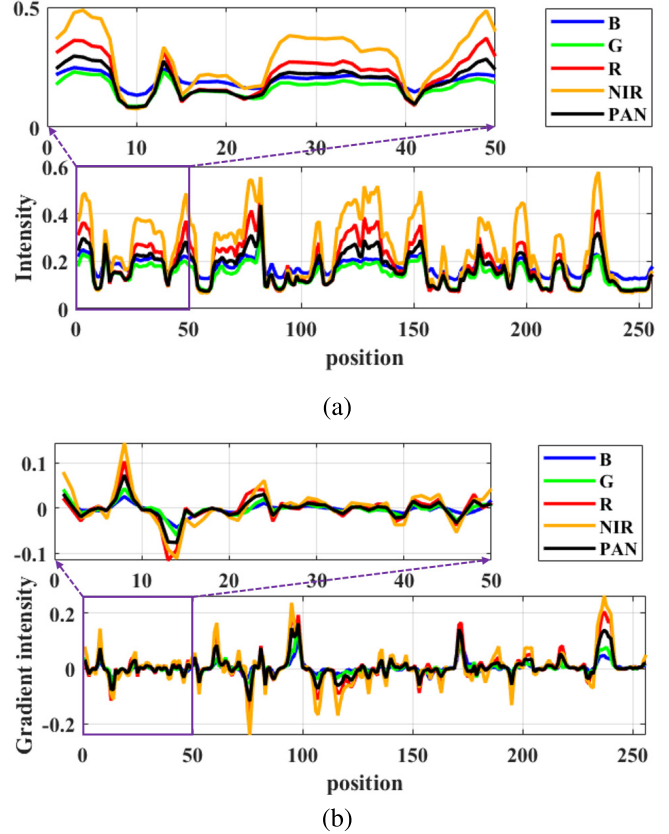


Fig. 2. (a) Plot of the intensity for both the PAN image and the HRMS data randomly choosing a row of the image. (b) Plot of the gradient intensity for both the PAN image and the HRMS data considering blue (B), green (G), red (R), and near-infrared (NIR) bands for the same row as in (a). It is worth to be remarked that the behavior of PAN and HRMS images is more similar in the gradient domain than in the intensity domain.

we propose a context-aware method for the following reasons. First, we found that the relationship between PAN and HRMS images in the gradient domain is closely related to the image context. To corroborate it, we chose a reduced resolution dataset to calculate the coefficients related to the HRMS

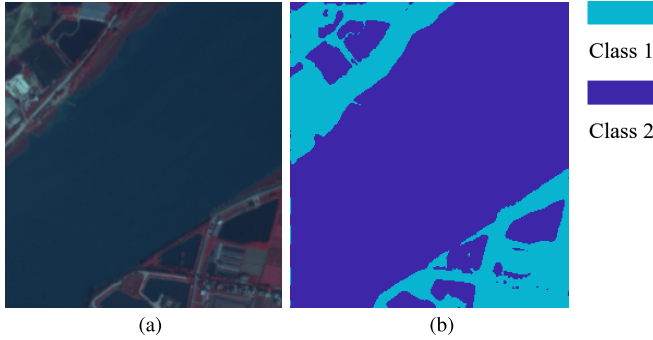


Fig. 3. (a) HRMS image. (b) Clustering of the coefficients related to the HRMS image in (a).

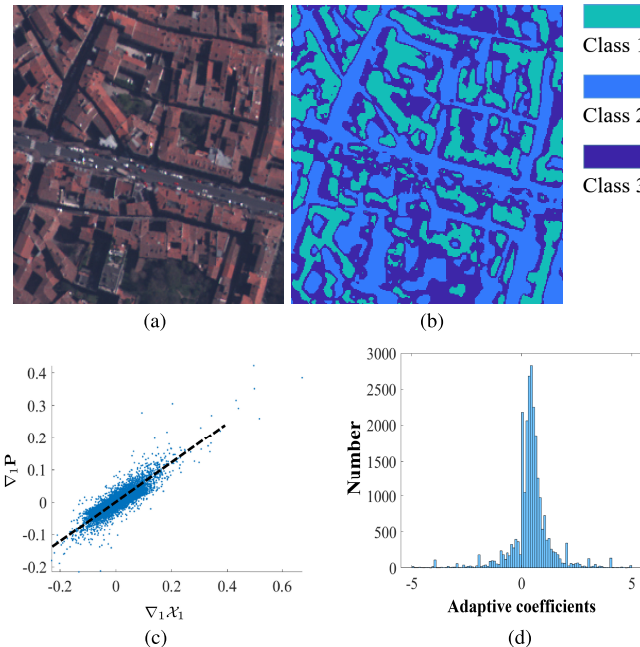


Fig. 4. (a) Close-up of the HRMS image of the Pléiades dataset. (b) Context-aware regions extracted from (a). (c) Scatter plot of $\nabla_1 X_1$ and $\nabla_1 P$ for pixels belonging to Class 1 in (b). (d) Histogram of $\nabla_1 X_1 \otimes \nabla_1 P$ for pixels belonging to Class 1 in (b). It is worth to be remarked that the distribution of $\nabla_1 X_1$ and $\nabla_1 P$ is well described by a directly proportional function, i.e., the black dotted line in (c). For other regions and bands, there is a similar directly proportional relationship between HRMS and PAN images in the gradient domain. Thus, the values of $\nabla X \otimes \nabla \bar{P}$ are approximately the same inside each region and each band.

and the PAN images in the gradient domain. Afterward, we clustered them. As shown in Fig. 3, there is a remarkable similarity between the clustered results and the image context in the original data. Second, a simple linear model can be exploited in this case to describe the relationship between each band of the HRMS image and the PAN image. Indeed, as shown in Fig. 4(c) and (d), the relationship between the PAN image and the HRMS image is approximately linear inside the same context-aware region. Therefore, the abovementioned observations motivate us to formulate the CDIF.

III. PROPOSED MODEL

A. Spectral Fidelity Term

Many previous methods directly upsample the MS image to obtain the same size image as the PAN image [43]. Thus, a fidelity term is built based on the upsampled version of the

MS image and the PAN image. However, the spectral content obtained by exploiting this fidelity term is often inaccurate. For this reason, we consider a different spectral fidelity term relied upon the following model:

$$\mathbf{X}\mathbf{B} = \mathbf{Y} + \xi_1 \quad (1)$$

where $\mathbf{B} \in \mathbb{R}^{HW \times HW}$ denotes a blurring matrix, $\mathbf{S} \in \mathbb{R}^{HW \times HW}$ represents the decimation operation, and ξ_1 indicates a zero-mean Gaussian noise. The blur operation is equivalent to the convolution of the HRMS image with the point spread function (PSF) of the MS sensor [44], [45]. According to (1), the spectral fidelity term can be expressed as

$$f_{\text{spec}} = \|\mathbf{X}\mathbf{B} - \mathbf{Y}\|_F^2 \quad (2)$$

where $\|\cdot\|_F$ is the Frobenius norm.

B. Proposed Context-Aware Details Injection Fidelity

For the pansharpening problem, fidelity terms are at the basis of each model extracting spatial and spectral information from the two inputs, i.e., the PAN and MS images. Many previous methods, e.g., [37] and [40], prefer exploring the global or local relationship between PAN and HRMS images in the gradient domain. However, we found that the relationship between PAN and HRMS images in the gradient domain can be better described in a context-aware manner (see Figs. 3 and 4). Therefore, we assume that

$$\nabla \mathbf{X} = \mathbf{G} \circ \nabla \bar{\mathbf{P}} + \xi_2 \quad (3)$$

where ∇ denotes the gradient operation along the two spatial directions, $\nabla \mathbf{X} \in \mathbb{R}^{S \times 2HW}$ stands for the mode-3 unfolding of $\nabla \mathcal{X}$, $\mathbf{G} \in \mathbb{R}^{S \times 2HW}$ represents the adaptive coefficients whose estimation is related to the image context, $\bar{\mathbf{P}}$ is the mode-3 unfolding of the extended PAN image (obtained by duplicating \mathbf{P} along the spectral direction), \circ indicates the Hadamard product, and ξ_2 is a zero-mean Gaussian noise. Hence, the CDIF is described by the following equation:

$$f_{\text{CDIF}} = \|\nabla \mathbf{X} - \mathbf{G} \circ \nabla \bar{\mathbf{P}}\|_F^2. \quad (4)$$

The CDIF with adaptive coefficients estimation is effective in extracting the features from the two inputs of the fusion process.

However, we cannot directly calculate \mathbf{G} by (3) because the HRMS image, \mathbf{X} , is what we want to find. Thus, the adaptive coefficients \mathbf{G} cannot be directly obtained by the following relationship:

$$\mathbf{G} = \nabla \mathbf{X} \otimes \nabla \bar{\mathbf{P}}. \quad (5)$$

To address this problem, we can exploit the MS image, \mathbf{Y} , which is instead known. We use an upsampling operation to simulate the inverse operation of the decimation operation, \mathbf{S} , and thus, we have that

$$\mathbf{X}\mathbf{B} \approx \tilde{\mathbf{Y}} = \Phi(\mathbf{Y}) \quad (6)$$

where $\tilde{\mathbf{Y}}$ denotes the mode-3 unfolding of the upsampled version of the MS image and $\Phi(\cdot)$ is the upsampling function implemented by considering a polynomial interpolator with 23 coefficients [46], commonly exploiting for pansharpening [2], [47]. Thus, the original relationship in (3) can

Algorithm 1 Estimation of the Adaptive Coefficients \mathbf{G}

Input: The upsampled version of the MS image, $\tilde{\mathbf{Y}}$, the extended PAN image, $\bar{\mathbf{P}}$, the number of clusters, k .

- 1: Calculate \mathbf{XB} via (6).
- 2: Calculate $\bar{\mathbf{PB}}$ via (8).
- 3: **for** $j = 1 \rightarrow k$ **do**
- 4: Calculate \mathbf{g}^j via (10).
- 5: **end for**

Output: \mathbf{G} collects \mathbf{g}^j for all the regions j .

be reported at reduced resolution considering the classical hypothesis performed in developing pancharpening algorithms, that is, the “invariance among scales.” Thus, we approximately have that

$$\nabla(\mathbf{XB}) \approx \mathbf{G} \circ \nabla(\bar{\mathbf{PB}}) \quad (7)$$

where

$$\bar{\mathbf{PB}} = \text{MTF}(\bar{\mathbf{P}}) \quad (8)$$

and $\text{MTF}(\cdot)$ is a Gaussian filter matched with the modulation transfer function (MTF) of the PAN image [2], [46], [48].

\mathbf{G} links the PAN image and the HRMS image. To estimate it, we search for similar pixels’ locations using a clustering method, i.e., the k -means clustering algorithm. The k -means approach needs to set the value of k (i.e., the number of clusters). To balance the computational burden and the clustering accuracy of the k -means algorithm, we set k to 5. Thus, all the pixels in the image are divided into k regions denoted by ω^j , $j = 1, 2, \dots, k$. As shown in Fig. 4(c), the values of the coefficients $\nabla\mathbf{X} \otimes \nabla\bar{\mathbf{P}}$ are approximately the same inside each region and for each band, which indicates that \mathbf{G} should have values around 1 considering (3). Accordingly, we have that

$$\mathbf{g}^j \circ \mathbf{c}^{(n)} = \mathbf{d}^{(n)} \quad \forall n \in \omega^j \quad (9)$$

where $\mathbf{c}^{(n)}$ and $\mathbf{d}^{(n)}$ are the pixels of $\nabla(\bar{\mathbf{PB}})$ and $\nabla(\mathbf{XB})$, respectively, inside region j , and \mathbf{g}^j denotes the adaptive coefficients for the j th region, i.e., \mathbf{G} evaluated for the j th region. The overdetermined equation (9) holds for all the pixels n belonging to the j th region, ω^j . The regression-based method, i.e., the ordinary least-squares, is selected to solve (9) for each spectral band. Therefore, we can estimate \mathbf{g}^j , as follows:

$$\mathbf{g}^j = \text{Reg}(\{\mathbf{d}^{(n)}, \mathbf{c}^{(n)}\}_{n \in \omega^j}) \quad (10)$$

where $\text{Reg}(\cdot, \cdot)$ denotes the ordinary least-squares regression using the inputs $\mathbf{d}^{(n)}$ and $\mathbf{c}^{(n)}$ for all $n \in \omega^j$ and separately applying it to all the spectral bands, thus estimating the coefficients of the vector \mathbf{g}^j [49].

Finally, \mathbf{G} is obtained by collecting \mathbf{g}^j (defined in (10)) for all the regions j . The adaptive coefficient process is summarized in Algorithm 1.

C. Total Variation Regularization

The total variation (TV) regularization is a conventional regularization term in the field of image processing [50]. This regularization can keep the piecewise constant of the result.

The anisotropic TV regularization at pixel (i, j, k) is defined as follows:

$$\begin{aligned} \|\nabla_1 \mathcal{X}(i, j, k)\|_1 &= \|\mathcal{X}(i+1, j, k) - \mathcal{X}(i, j, k)\|_1 \\ \|\nabla_2 \mathcal{X}(i, j, k)\|_1 &= \|\mathcal{X}(i, j+1, k) - \mathcal{X}(i, j, k)\|_1 \\ \|\nabla_3 \mathcal{X}(i, j, k)\|_1 &= \|\mathcal{X}(i, j, k+1) - \mathcal{X}(i, j, k)\|_1. \end{aligned} \quad (11)$$

We apply TV regularization to describe the properties of the HRMS images, i.e., the piecewise constant and the sparsity in the gradient domain. The TV regularization term is given as follows:

$$f_{\text{TV}} = \beta_1 \|\nabla_1 \mathbf{X}\|_1 + \beta_2 \|\nabla_2 \mathbf{X}\|_1 + \beta_3 \|\nabla_3 \mathbf{X}\|_1 \quad (12)$$

where $\nabla_i \mathbf{X}$ is the mode-3 unfolding of $\nabla_i \mathcal{X}$, and β_1 , β_2 , and β_3 are positive parameters.

D. Proposed Model

Combining the abovementioned terms, the final model can be expressed as

$$\begin{aligned} \min_{\mathbf{X}} \|\mathbf{XB} - \mathbf{Y}\|_F^2 + \lambda \|\nabla \mathbf{X} - \mathbf{G} \circ \nabla \bar{\mathbf{P}}\|_F^2 \\ + \beta_1 \|\nabla_1 \mathbf{X}\|_1 + \beta_2 \|\nabla_2 \mathbf{X}\|_1 + \beta_3 \|\nabla_3 \mathbf{X}\|_1. \end{aligned} \quad (13)$$

This model is convex, but the direct calculation requires a huge computational burden. Thus, we designed an algorithm based on the ADMM [42] framework.

IV. PROPOSED ALGORITHM

The ADMM [42] framework is one of the widely used methods to solve structured convex optimization problems. We designed a fast and effective ADMM-based algorithm to solve the proposed model. Let us introduce the auxiliary variables \mathbf{U} , \mathbf{H}_1 , \mathbf{H}_2 , and \mathbf{H}_3 , where $\mathbf{U} = \mathbf{XB}$, $\mathbf{H}_1 = \nabla_1 \mathbf{X}$, $\mathbf{H}_2 = \nabla_2 \mathbf{X}$, and $\mathbf{H}_3 = \nabla_3 \mathbf{X}$. The optimization model can be reconstructed as

$$\begin{aligned} \min_{\mathbf{X}, \mathbf{U}, \mathbf{H}_1, \mathbf{H}_2, \mathbf{H}_3} \quad & \|\mathbf{US} - \mathbf{Y}\|_F^2 + \lambda \|\nabla \mathbf{X} - \mathbf{G} \circ \nabla \bar{\mathbf{P}}\|_F^2 \\ & + \beta_1 \|\mathbf{H}_1\|_1 + \beta_2 \|\mathbf{H}_2\|_1 + \beta_3 \|\mathbf{H}_3\|_1 \\ \text{s.t.} \quad & \mathbf{U} = \mathbf{XB}, \quad \mathbf{H}_1 = \nabla_1 \mathbf{X} \\ & \mathbf{H}_2 = \nabla_2 \mathbf{X}, \quad \mathbf{H}_3 = \nabla_3 \mathbf{X}. \end{aligned} \quad (14)$$

Thus, the augmented Lagrangian function is given as follows:

$$\begin{aligned} \mathcal{L} = \|\mathbf{US} - \mathbf{Y}\|_F^2 + \lambda \|\nabla \mathbf{X} - \mathbf{G} \circ \nabla \bar{\mathbf{P}}\|_F^2 \\ + \frac{\eta_1}{2} \left\| \mathbf{XB} - \mathbf{U} + \frac{\Lambda_1}{\eta_1} \right\|_F^2 \\ + \beta_1 \|\mathbf{H}_1\|_1 + \beta_2 \|\mathbf{H}_2\|_1 + \beta_3 \|\mathbf{H}_3\|_1 \\ + \frac{\eta_2}{2} \left\| \nabla_1 \mathbf{X} - \mathbf{H}_1 + \frac{\Lambda_2}{\eta_2} \right\|_F^2 \\ + \frac{\eta_3}{2} \left\| \nabla_2 \mathbf{X} - \mathbf{H}_2 + \frac{\Lambda_3}{\eta_3} \right\|_F^2 \\ + \frac{\eta_4}{2} \left\| \nabla_3 \mathbf{X} - \mathbf{H}_3 + \frac{\Lambda_4}{\eta_4} \right\|_F^2 + \text{const} \end{aligned} \quad (15)$$

where Λ_1 , Λ_2 , Λ_3 , and Λ_4 represent the Lagrange multipliers, and const denotes a constant that is independent of the variables \mathbf{U} , \mathbf{X} , and \mathbf{H}_i , $i = 1, 2, 3$. The optimization problem is solved by dealing with five subproblems. Each subproblem is solved by minimizing one variable under the condition that the others are fixed.

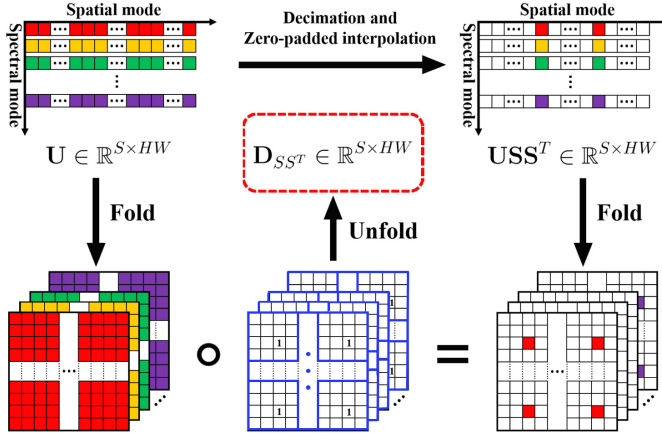


Fig. 5. Graphic representation of (22) for a scale ratio equal to 4. The white squares with a blank content indicate zero values. The first row shows the processing from \mathbf{U} to \mathbf{USS}^T , which is equal to an elementwise multiplication between $\mathbf{D}_{\mathbf{SS}^T}$ and \mathbf{U} , i.e., the second row. It is worth noting that $\mathbf{D}_{\mathbf{SS}^T}$ is produced from sparse matrices (i.e., the blue squares), whose entries are 1 only in one position [44].

A. X-Subproblem

According to (15), the \mathbf{X} -subproblem is expressed as the following optimization problem:

$$\begin{aligned} \min_{\mathbf{X}} \lambda \|\nabla \mathbf{X} - \mathbf{G} \circ \nabla \bar{\mathbf{P}}\|_F^2 + \frac{\eta_1}{2} \left\| \mathbf{X}\mathbf{B} - \mathbf{U} + \frac{\Lambda_1}{\eta_1} \right\|_F^2 \\ + \frac{\eta_2}{2} \left\| \nabla_1 \mathbf{X} - \mathbf{H}_1 + \frac{\Lambda_2}{\eta_2} \right\|_F^2 + \frac{\eta_3}{2} \left\| \nabla_2 \mathbf{X} - \mathbf{H}_2 + \frac{\Lambda_3}{\eta_3} \right\|_F^2 \\ + \frac{\eta_4}{2} \left\| \nabla_3 \mathbf{X} - \mathbf{H}_3 + \frac{\Lambda_4}{\eta_4} \right\|_F^2. \end{aligned} \quad (16)$$

There are only Frobenius norms in the optimization model above. Thus, it can be solved by the fast Fourier transform (FFT) algorithm under the periodic boundary condition

$$\mathbf{X}^{k+1} := \mathcal{F}^{-1} \left(\frac{\mathcal{F}(\mathbf{W}^k + \mathbf{Q}^k)}{\mathcal{F}(\mathbf{O})} \right) \quad (17)$$

with

$$\mathbf{W}^k = 2\lambda \nabla^T (\mathbf{G} \circ \nabla \bar{\mathbf{P}}) + \eta_1 \mathbf{U}^k \mathbf{B}^T + \sum_{i=2}^4 (\eta_i \nabla_{i-1}^T \mathbf{H}_{i-1}^k) \quad (18)$$

$$\mathbf{Q}^k = -\Lambda_1^k \mathbf{B}^T - \sum_{i=2}^4 (\nabla_{i-1}^T \Lambda_i^k) \quad (19)$$

$$\mathbf{O} = 2\lambda \nabla^T \nabla + \eta_1 \mathbf{B} \mathbf{B}^T + \sum_{i=2}^4 \eta_i \nabla_{i-1}^T \nabla_{i-1} \quad (20)$$

where $\mathcal{F}(\cdot)$ and $\mathcal{F}^{-1}(\cdot)$ denote the fast Fourier transform and its inverse transformation, respectively, $(\cdot)^T$ is the transpose operator, and the division is elementwise.

B. U-Subproblem

The \mathbf{U} -subproblem is given as follows:

$$\min_{\mathbf{U}} \|\mathbf{US} - \mathbf{Y}\|_F^2 + \frac{\eta_1}{2} \left\| \mathbf{XB} - \mathbf{U} + \frac{\Lambda_1}{\eta_1} \right\|_F^2. \quad (21)$$

Algorithm 2 ADMM-Based Solver for the Proposed Pan-sharpening Model (13)

Input: The MS image, \mathbf{Y} , the extended PAN image, $\bar{\mathbf{P}}$, the adaptive coefficients, \mathbf{G} , λ , β_1 , β_2 , β_3 , η_1 , η_2 , η_3 , η_4 , r , k_{mit} , and ε .

Initialization: $\mathbf{X}^0 = \Psi(\mathbf{Y}, r)$, $\mathbf{U}^0 = \Lambda_1^0 = \mathbf{0}$, $\mathbf{H}_1^0 = \mathbf{H}_2^0 = \mathbf{H}_3^0 = \Lambda_2^0 = \Lambda_3^0 = \Lambda_4^0 = \mathbf{0}$, $k = 0$

- 1: **while** $k < k_{\text{mit}}$ and $\text{RelCha} > \varepsilon$ **do**
- 2: Update \mathbf{X}^{k+1} via (17).
- 3: Update \mathbf{U}^{k+1} via (23).
- 4: Update \mathbf{H}_i^{k+1} via (25), $i=1,2,3$.
- 5: Update Lagrange multiplier Λ_j^{k+1} via (26), $j=1,2,3,4$.
- 6: $k = k + 1$.
- 7: **end while**

Output: The fused HRMS image \mathbf{X}

The solution to this optimization problem relies on handling the decimation operation, \mathbf{S} . \mathbf{USS}^T can be seen as an elementwise multiplication $\mathbf{D}_{\mathbf{SS}^T}$ on \mathbf{U}

$$\mathbf{USS}^T = \mathbf{U} \circ \mathbf{D}_{\mathbf{SS}^T} \quad (22)$$

as shown in Fig. 5 [44]. Thus, the method based on the elementwise division can efficiently solve the \mathbf{U} -subproblem

$$\mathbf{U}^{k+1} := \frac{2\mathbf{YS}^T + \eta_1 \mathbf{X}^{k+1} \mathbf{B} + \Lambda_1^k}{2\mathbf{D}_{\mathbf{SS}^T} + \eta_1 \mathbf{1}}. \quad (23)$$

C. \mathbf{H}_i -Subproblem

For \mathbf{H}_i -subproblems, the optimization problem can be formalized as follows:

$$\min_{\mathbf{H}_i} \frac{\eta_{i+1}}{2} \left\| \nabla_i \mathbf{X} - \mathbf{H}_i + \frac{\Lambda_{i+1}}{\eta_{i+1}} \right\|_F^2 + \beta_i \|\mathbf{H}_i\|_1. \quad (24)$$

The above problem can be solved by the soft-thresholding strategy [51]. Thus, we have that

$$\mathbf{H}_i^{k+1} = \text{Soft} \left(\mathbf{X}^{k+1} + \frac{\Lambda_{i+1}^k}{\eta_{i+1}}, \frac{\beta_i}{\eta_{i+1}} \right) \quad (25)$$

where $\text{Soft}(a, b) := \text{sign}(a) \cdot \max(|a| - b, 0)$, $i = 1, 2, 3$.

D. Updating Multipliers

Finally, the multipliers Λ_1 , Λ_2 , Λ_3 , and Λ_4 are updated as follows:

$$\begin{pmatrix} \Lambda_1^{k+1} \\ \Lambda_2^{k+1} \\ \Lambda_3^{k+1} \\ \Lambda_4^{k+1} \end{pmatrix} := \begin{pmatrix} \Lambda_1^k \\ \Lambda_2^k \\ \Lambda_3^k \\ \Lambda_4^k \end{pmatrix} + \begin{pmatrix} \eta_1 (\mathbf{X}^{k+1} \mathbf{B} - \mathbf{U}^{k+1}) \\ \eta_2 (\nabla_1 \mathbf{X}^{k+1} - \mathbf{H}_1^{k+1}) \\ \eta_3 (\nabla_2 \mathbf{X}^{k+1} - \mathbf{H}_2^{k+1}) \\ \eta_4 (\nabla_3 \mathbf{X}^{k+1} - \mathbf{H}_3^{k+1}) \end{pmatrix}. \quad (26)$$

The reconstructed model, i.e., (14), is convex for each variable satisfying the hypotheses under the convergence theorem in [42]. Therefore, the convergence of the whole algorithm can be guaranteed. The relative change (RelCha) and the number of iterations are used as termination conditions of the algorithm. The RelCha is defined as

$$\text{RelCha} = \|\mathbf{X}^{k+1} - \mathbf{X}^k\|_F / \|\mathbf{X}^k\|_F. \quad (27)$$

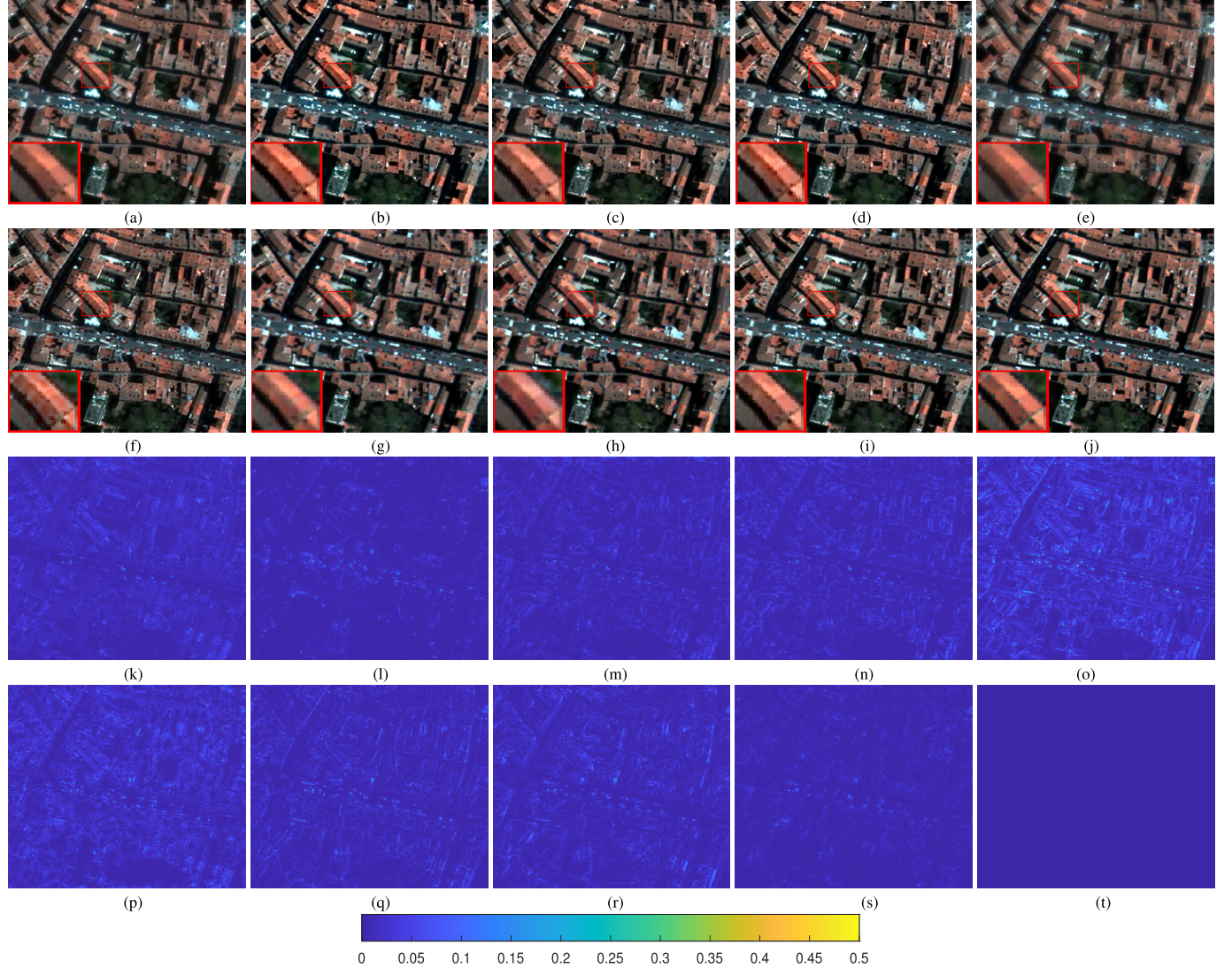


Fig. 6. Fusion results with close-ups for the compared approaches on the four-band Pléiades dataset at reduced resolution (size of the PAN image: 256×256). Visual results in true colors of (a) PRACS [9], (b) RBDSD [49], (c) C-GLP [59], (d) GLP-Reg-FS [43], (e) LGC [37], (f) HQBP [60], (g) PNN [19], (h) TPNN [61], (i) proposed method, and (j) ground-truth (GT). Residual images for the displayed red band: (k) PRACS [9], (l) RBDSD [49], (m) C-GLP [59], (n) GLP-Reg-FS [43], (o) LGC [37], (p) HQBP [60], (q) PNN [19], (r) TPNN [61], (s) proposed, and (t) GT.

The whole optimization algorithm can be summarized in Algorithm 2, where k_{mit} denotes the maximum iteration, r is the scale ratio between MS and PAN images, ε is a tolerance value, and Ψ denotes the bicubic interpolation.

V. EXPERIMENTAL RESULTS

This section is devoted to the demonstration of the effectiveness of the proposed algorithm. We compare the proposed method with some state-of-the-art methods on data coming from different sensors, i.e., IKONOS, QuickBird, Pléiades, WorldView-2, and WorldView-3. To make the experimental analysis more representative, we chose methods from different pansharpening classes. Two assessment procedures, i.e., at reduced resolution and at full resolution, are considered in this article to show the high performance of the proposed approach. All the methods in the benchmark are run on the same software and hardware platforms, i.e., MATLAB (R2016b), a computer of 16-Gb RAM with AMD Ryzen7-4800H, NVIDIA GeForce GTX 1650, and Radeon

Graphics 2.90 GHz. The procedure to adjust the parameters is also described in this section together with an ablation study in Section V-E, even comparing the proposed approach with the direct estimation and the equivalent methodology based on patches. It is worth to be remarked that k_{mit} , r , and ε are set to 100, 4, and 2×10^{-5} , respectively, in all the experiments.

A. Quality Metrics

There are many metrics to quantitatively measure the performance at reduced resolution and full resolution. We use the peak signal-to-noise ratio (PSNR) [52], the structural similarity index (SSIM) [52], the spectral angle mapper (SAM) [53], the spatial correlation coefficient (SCC) [54], the erreur relative globale adimensionnelle de synthèse (ERGAS) [55], and the Q2ⁿ index [56], [57] (i.e., the Q4 for four-band MS images or the Q8 for eight-band MS data) for the assessment at reduced resolution. Instead, at full resolution, where no reference image is available for validation, the quality with no reference (QNR) [58] index consisting of a spectral quality index, D_λ , and a spatial quality index, D_s , is adopted.

B. Benchmark

We compare the proposed technique with some state-of-the-art pansharpening approaches. For CS methods, we choose for comparison the PRACS [9] and the robust BDSD (RBDSD) [49]. The GLP framework is a widely used approach for MRA methods. In this class, the context-based GLP (C-GLP) [59] and the GLP with a full scale regression model (GLP-Reg-FS) [43] are considered. Moreover, the compared methods also include the VO method with LGC [37], the high-quality Bayesian pansharpening (HQBP) [60], and the pansharpening neural network (PNN) [19] and its target-adaptive version (TPNN) [61]. It is worth to be noted that we used the PNN and the TPNN distributed in [1] with parameters shared by the authors. All compared methods are summarized as follows.

- 1) *CS Methods*: PRACS [9] and RBDSD [49].
- 2) *MRA Methods*: C-GLP [59] and GLP-Reg-FS [43].
- 3) *VO Methods*: LGC [37] and HQBP [60].
- 4) *ML Methods*: PNN [19] and TPNN [61].

C. Reduced Resolution Assessment

This section is devoted to the comparison of the proposed method with the adopted benchmark on data at reduced resolution.

1) *Pléiades Test Case*: The Pléiades dataset consists of two images (the PAN image and the four-band MS image with a spatial resolution of 0.5 and 2 m, respectively) acquired by the Pléiades satellite mission. The results are shown in Fig. 6. The images in Fig. 6(a), (e), and (g) introduce some spatial artifacts. Moreover, the images in Fig. 6(b), (h), and (i), especially the one obtained by the proposed method, can effectively alleviate the spectral and spatial distortions. The residual images are depicted in Fig. 6(k)–(t). It is easy to see that the proposed method gets the best results compared with the other approaches [see Fig. 6(s)]. Table I reports the quantitative comparison for the different methods. These results corroborate the abovementioned analysis showing that the proposed method gets the best index values with respect to the techniques in the proposed benchmark.

2) *QuickBird Test Case*: The QuickBird dataset consists of a PAN image (spatial resolution of 0.7 m) and four MS bands (spatial resolution of 2.8 m) captured in the visible near-infrared (NIR) spectrum. Fig. 7 depicts the fused results obtained by the compared approaches. Fig. 7(a), (e), and (f) are fuzzier than the others and characterized by an evident spatial distortion. Instead, Fig. 7(g) has greater spatial accuracy but paying it with a relevant spectral distortion. Fig. 7(b), (h), and (i) have a better visual appearance compared with the other images. By observing the small red box in the upper left corner of the picture, the proposed method can better represent the edges of the houses. Moreover, the residuals in Fig. 7 point out the superiority of the proposed method. The best result is shown in Fig. 7(s), especially having a look at the upper left area of the image. Finally, Table II reports the quantitative comparison among the methods in the benchmark. Again, it corroborates the previous analysis. Indeed, the proposed method shows the best indexes in Table II.

TABLE I

QUANTITATIVE RESULTS FOR THE TEST CASE IN FIG. 6. TPNN [61] IS EXECUTED ON GPU (G). (BOLD: BEST; UNDERLINE: SECOND BEST)

Method	PSNR	SSIM	SAM	SCC	ERGAS	Q4	Time(s)
PRACS [9]	33.36	0.926	4.106	0.968	3.167	0.890	0.046
RBDSD [49]	<u>36.16</u>	<u>0.960</u>	<u>3.276</u>	<u>0.975</u>	<u>2.409</u>	0.941	<u>0.044</u>
C-GLP [59]	34.33	0.937	4.456	0.963	2.980	0.958	0.336
GLP-Reg-FS [43]	35.14	0.954	3.411	0.970	2.582	0.914	0.038
LGC [37]	31.98	0.910	3.897	0.958	3.595	0.918	7.722
HQBP [60]	33.62	0.918	4.456	0.965	3.055	0.946	13.38
PNN [19]	35.36	0.952	3.245	0.973	2.505	0.969	12.04
TPNN [61]	35.24	0.950	3.292	0.973	2.511	<u>0.968</u>	0.065(G)
Proposed	37.35	0.965	2.884	0.981	2.040	0.978	13.44
Ideal value	$+\infty$	1	0	1	0	1	-

TABLE II

QUANTITATIVE RESULTS FOR THE TEST CASE IN FIG. 7. TPNN [61] IS EXECUTED ON GPU (G). (BOLD: BEST; UNDERLINE: SECOND BEST)

Method	PSNR	SSIM	SAM	SCC	ERGAS	Q4	Time(s)
PRACS [9]	29.51	0.797	7.964	0.885	8.701	0.758	<u>0.071</u>
RBDSD [49]	30.46	0.814	8.150	0.898	<u>7.795</u>	0.778	0.064
C-GLP [59]	30.20	0.815	<u>7.246</u>	0.892	8.040	0.805	0.800
GLP-Reg-FS [43]	30.43	0.821	7.774	0.901	7.799	0.784	0.075
LGC [37]	29.52	0.788	7.659	0.884	8.737	0.761	9.797
HQBP [60]	30.23	0.795	8.807	0.897	7.994	0.768	13.35
PNN [19]	30.78	0.840	7.843	0.910	7.452	0.798	0.281
TPNN [61]	<u>31.12</u>	<u>0.845</u>	7.326	<u>0.914</u>	<u>7.246</u>	<u>0.828</u>	0.138(G)
Proposed	31.54	0.852	6.792	0.922	6.896	0.849	12.60
Ideal value	$+\infty$	1	0	1	0	1	-

TABLE III

QUANTITATIVE RESULTS FOR THE TEST CASE IN FIG. 8. TPNN [61] IS EXECUTED ON GPU (G). (BOLD: BEST; UNDERLINE: SECOND BEST)

Method	PSNR	SSIM	SAM	SCC	ERGAS	Q4	Time(s)
PRACS [9]	38.98	0.935	3.476	0.922	3.833	0.851	0.347
RBDSD [49]	<u>40.08</u>	<u>0.954</u>	2.598	0.930	<u>2.988</u>	<u>0.909</u>	0.234
C-GLP [59]	38.14	0.924	3.275	0.896	3.976	0.818	2.815
GLP-Reg-FS [43]	39.66	0.950	2.848	0.924	3.177	0.896	<u>0.182</u>
LGC [37]	37.69	0.916	3.375	0.899	4.261	0.784	47.67
HQBP [60]	38.18	0.925	3.486	0.896	3.989	0.835	41.96
PNN [19]	39.50	0.953	3.204	<u>0.934</u>	3.357	0.912	0.443
TPNN [61]	38.10	0.929	3.390	0.887	4.054	0.842	0.090 (G)
Proposed	40.47	0.956	<u>2.589</u>	0.937	2.964	0.907	47.27
Ideal value	$+\infty$	1	0	1	0	1	-

3) *IKONOS Toulouse Test Case*: The IKONOS Toulouse dataset consists of a PAN image (spatial resolution of 1 m) and a four-band MS image (spatial resolution of 4 m) acquired by the IKONOS sensor in the visible NIR spectrum over the city of Toulouse, France. The visual results are shown in Fig. 8. Fig. 8(c) and (e) suffer from spectral distortions, and Fig. 8(e), (f), and (h) are affected by spatial distortions. Instead, in Fig. 8(b) and (i), the best results are shown. Table III reports the quantitative results pointing out that the proposed approach is always in the first two positions in the ranking.

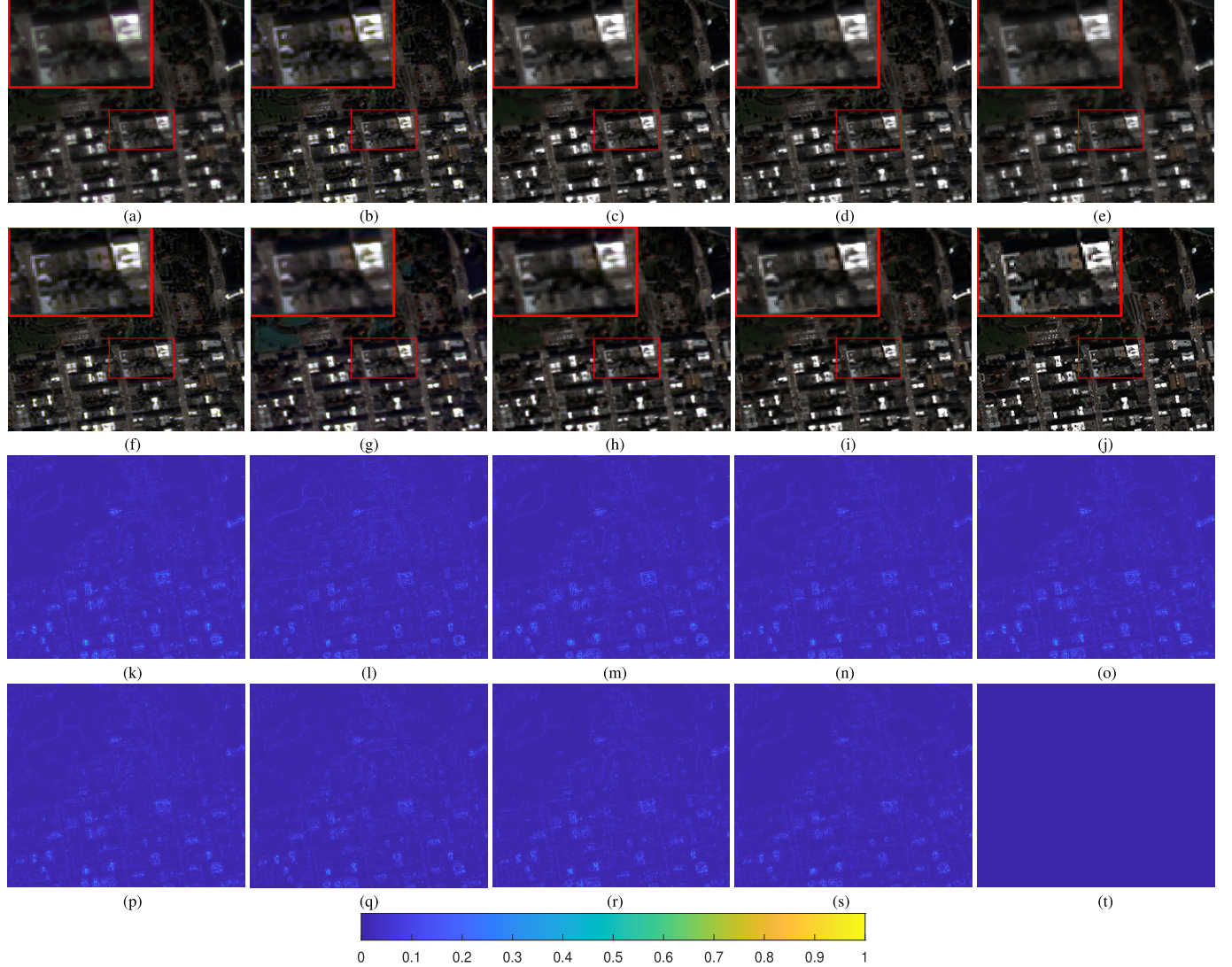


Fig. 7. Fusion results with close-ups for the compared approaches on the four-band QuickBird dataset at reduced resolution (size of the PAN image: 256×256). Visual results in true colors of (a) PRACS [9], (b) RBDSD [49], (c) C-GLP [59], (d) GLP-Reg-FS [43], (e) LGC [37], (f) HQBP [60], (g) PNN [19], (h) TPNN [61], (i) proposed method, and (j) GT, respectively. Residual images for the displayed red band: (k) PRACS [9], (l) RBDSD [49], (m) C-GLP [59], (n) GLP-Reg-FS [43], (o) LGC [37], (p) HQBP [60], (q) PNN [19], (r) TPNN [61], (s) proposed, and (t) GT.

4) WorldView-3 Test Case: The WorldView-3 dataset consists of two images: a PAN image with a spatial resolution of 0.31 m and an eight-band MS image with a spatial resolution of 1.24 m acquired by the WorldView-3 sensor in the visible NIR spectrum. Fig. 9(a)–(j) shows the true colors images of the fused products. It is clear to see that the proposed method obtains more details than the other approaches. In Fig. 9(a), (c), (f), and (g), some spatial details are missing, as shown by the related close-ups in the figures. Instead, Fig. 9(b), (e), and (h) depicts some spatial artifacts in the vegetated area. Comparing the fused products with the ground truth (GT), we can observe that the proposed method achieves good results. Residual images can better visualize the differences among the compared approaches [see Fig. 9(k)–(t)]. It is easy to see that the edges of the houses in the scenario under test make several problems among the compared approaches. However, the proposed method still shows better results than the others, as further testified by the numerical results in Table IV.

D. Full-Resolution Assessment

We conduct some experiments on data at full resolution to further assess the proposed method.

1) IKONOS Sichuan Test Case: The IKONOS Sichuan dataset consists of a PAN image and a four-band MS image acquired by the IKONOS sensor over the Sichuan region in China. The size of the PAN image is 512×576 . The results of the methods in the benchmark are displayed in Fig. 10. The proposed method is still valid for these four-band data at full resolution. Because of the absence of a GT image, the QNR index is calculated. As shown in Table V, the proposed method can get the best overall accuracy, as measured by the QNR index.

2) WorldView-2 Test Case: The WorldView-2 dataset is a full-resolution set of data consisting of a PAN and an eight-band MS data acquired by the WorldView-2 sensor. The MS image is acquired in the visible NIR with a spatial resolution of 1.84 m, and the PAN image (depicted in Fig. 11) has a spatial resolution of 0.46 m. The size of the PAN image

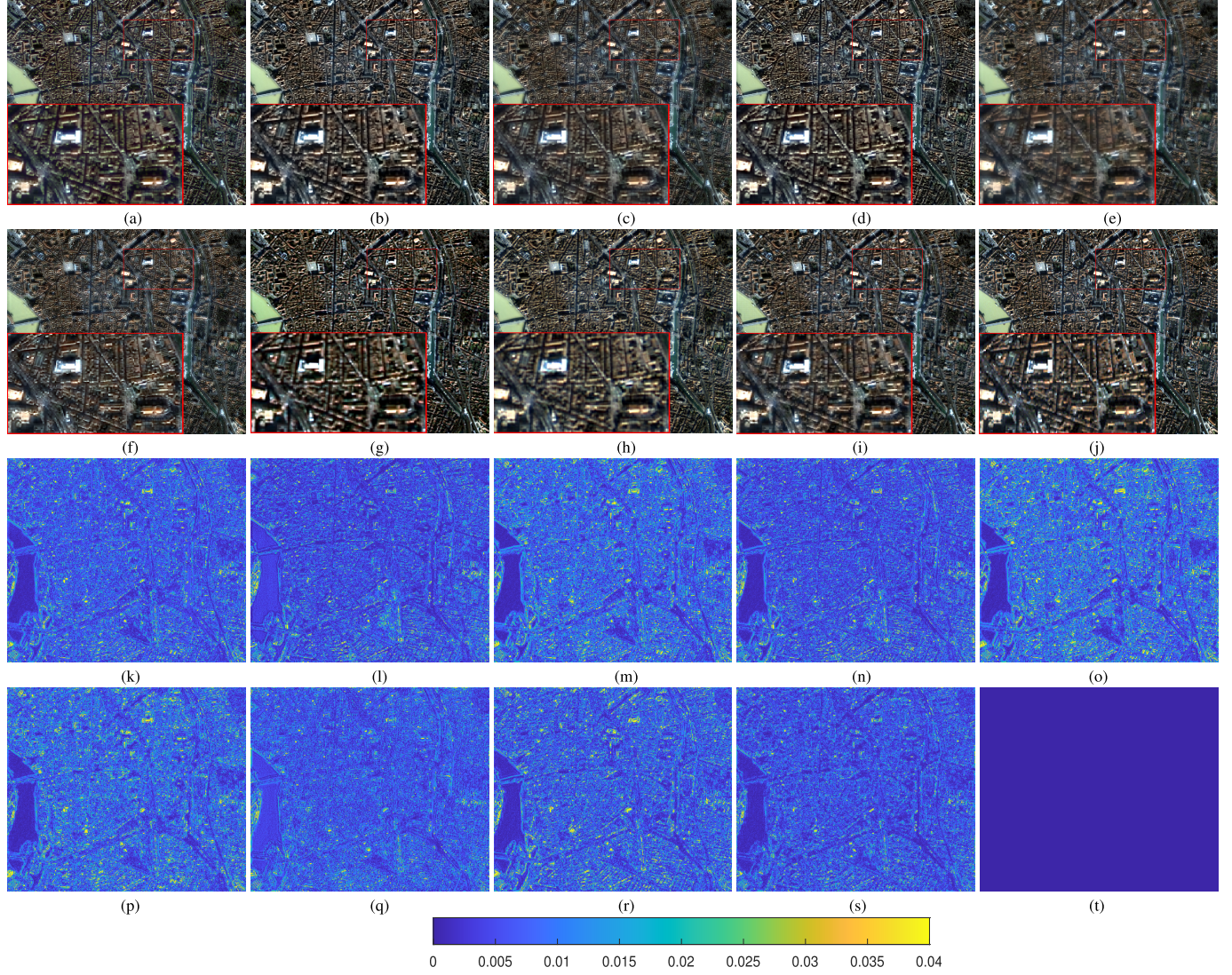


Fig. 8. Fusion results with close-ups for the compared approaches on the four-band IKONOS Toulouse dataset at reduced resolution (size of the PAN image: 512×512). Visual results in true colors of (a) PRACS [9], (b) RBDSD [49], (c) C-GLP [59], (d) GLP-Reg-FS [43], (e) LGC [37], (f) HQBP [60], (g) PNN [19], (h) TPNN [61], (i) proposed method, and (j) GT, respectively. Residual images for the displayed red band: (k) PRACS [9], (l) RBDSD [49], (m) C-GLP [59], (n) GLP-Reg-FS [43], (o) LGC [37], (p) HQBP [60], (q) PNN [19], (r) TPNN [61], (s) proposed, and (t) GT.

TABLE IV

QUANTITATIVE RESULTS FOR THE TEST CASE IN FIG. 9. TPNN [61] IS EXECUTED ON GPU (G). (BOLD: BEST; UNDERLINE: SECOND BEST)

Method	PSNR	SSIM	SAM	SCC	ERGAS	Q8	Time(s)
PRACS [9]	31.55	0.837	8.547	0.927	5.677	0.929	0.157
RBDSD [49]	32.24	0.858	8.540	0.936	5.214	<u>0.907</u>	0.103
C-GLP [59]	32.16	0.861	7.624	0.938	5.230	0.865	1.207
GLP-Reg-FS [43]	31.89	0.845	8.385	0.932	5.479	0.876	<u>0.132</u>
LGC [37]	31.24	0.845	7.082	0.930	5.713	0.832	17.24
HQBP [60]	30.79	0.808	7.924	0.918	6.117	0.819	24.47
PNN [19]	30.80	0.876	9.184	0.941	5.546	0.849	0.190
TPNN [61]	<u>32.50</u>	<u>0.885</u>	6.520	<u>0.945</u>	<u>4.852</u>	0.872	0.139(G)
Proposed	33.30	0.896	<u>6.538</u>	0.951	4.558	0.899	28.97
Ideal value	$+\infty$	1	0	1	0	1	-

is 256×256 . The fusion results are displayed in Fig. 11. The proposed method gets better results than the others. Indeed, by comparing it with the PAN image, the spatial details are

well preserved. About the quantitative results, our approach gets the best values for all the considered metrics, as shown in Table VI.

E. Discussion

1) *Analysis of Parameters:* In this section, we analyze the parameters used in the proposed approach. Although there are many parameters, some similarities between the spatial dimensions of the TV regularization can be found. We can assume that $\beta_1 = \beta_2$ and $\eta_2 = \eta_3$ for fine-tuning the parameters in an easier way. For a better visualization, the metrics are normalized by $(\text{metric} - \text{Mean}(\text{metric})) / \text{Std}(\text{metric})$, where $\text{Mean}(\cdot)$ denotes the averaging operation and $\text{Std}(\cdot)$ denotes the standard deviation operation. We only adjust one parameter at a time, thus having all the others fixed. The test is performed by using the Pléiades dataset. As shown in Fig. 12, the parameters λ and η_1 are more sensitive than the others. Thus, we can fine-tune first the parameters λ and η_1 , then adjusting the others. The parameters can be quickly fixed in this way,

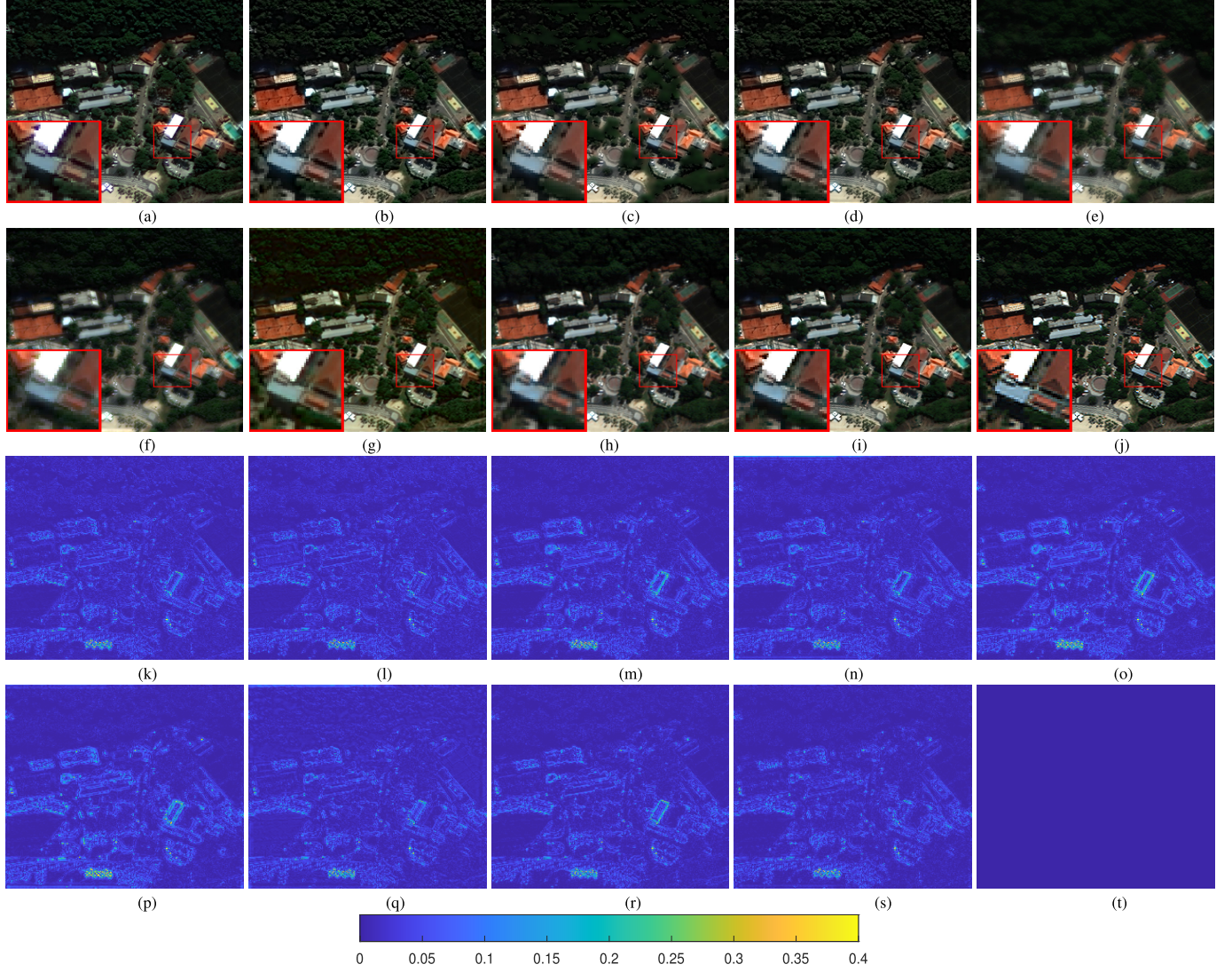


Fig. 9. Fusion results with close-ups for the compared approaches on the eight-band WorldView-3 dataset at reduced resolution (size of the PAN image: 256×256). Visual results in true colors of (a) PRACS [9], (b) RBDSD [49], (c) C-GLP [59], (d) GLP-Reg-FS [43], (e) LGC [37], (f) HQBP [60], (g) PNN [19], (h) TPNN [61], (i) proposed method, and (j) GT, respectively. Residual images for the displayed red band: (k) PRACS [9], (l) RBDSD [49], (m) C-GLP [59], (n) GLP-Reg-FS [43], (o) LGC [37], (p) HQBP [60], (q) PNN [19], (r) TPNN [61], (s) proposed, and (t) GT.

TABLE V

QUANTITATIVE RESULTS FOR THE TEST CASE IN FIG. 10. TPNN [61] IS EXECUTED ON GPU (G). (BOLD: BEST; UNDERLINE: SECOND BEST)

Method	D_λ	D_s	QNR	Time(s)
PRACS [9]	0.029	0.249	0.730	0.419
RBDSD [49]	0.086	0.396	0.552	0.285
C-GLP [59]	0.032	0.076	0.895	3.948
GLP-Reg-FS [43]	0.096	0.274	0.656	<u>0.184</u>
LGC [37]	0.008	0.157	0.837	60.57
HQBP [60]	0.063	0.106	0.838	68.77
PNN [19]	0.094	0.267	0.663	0.332
TPNN [61]	<u>0.012</u>	<u>0.026</u>	<u>0.963</u>	0.125(G)
Proposed	0.020	0.010	0.970	54.76
Ideal value	0	0	1	-

even if we have eight parameters in our model. Considering the best point to balance all the different metrics, we selected the following set of parameters to be used in our experimental analysis: $\lambda = 5 \times 10^{-5}$, $\eta_1 = 1 \times 10^{-4}$, $\beta_1 = \beta_2 = 1 \times 10^{-7}$, $\eta_2 = \eta_3 = 1 \times 10^{-3}$, $\beta_3 = 1 \times 10^{-5}$, and $\eta_4 = 5 \times 10^{-8}$.

TABLE VI

QUANTITATIVE RESULTS FOR THE TEST CASE IN FIG. 11. TPNN [61] IS EXECUTED ON GPU (G). (BOLD: BEST; UNDERLINE: SECOND BEST)

Method	D_λ	D_s	QNR	Time(s)
PRACS [9]	<u>0.012</u>	0.091	0.898	0.395
RBDSD [49]	0.028	0.041	0.932	0.325
C-GLP [59]	0.025	0.090	0.887	1.386
GLP-Reg-FS [43]	0.070	0.104	0.833	<u>0.180</u>
LGC [37]	0.016	0.060	0.925	53.49
HQBP [60]	0.031	<u>0.019</u>	<u>0.951</u>	65.89
PNN [19]	0.121	0.047	0.839	0.323
TPNN [61]	0.041	0.029	0.931	0.164(G)
Proposed	0.011	0.014	0.975	72.80
Ideal value	0	0	1	-

2) *Ablation Study*: The proposed model consists of the CDIF, the spectral fidelity term, and the conventional TV regularization. To analyze the role of these three different parts, the following three submodels are considered.

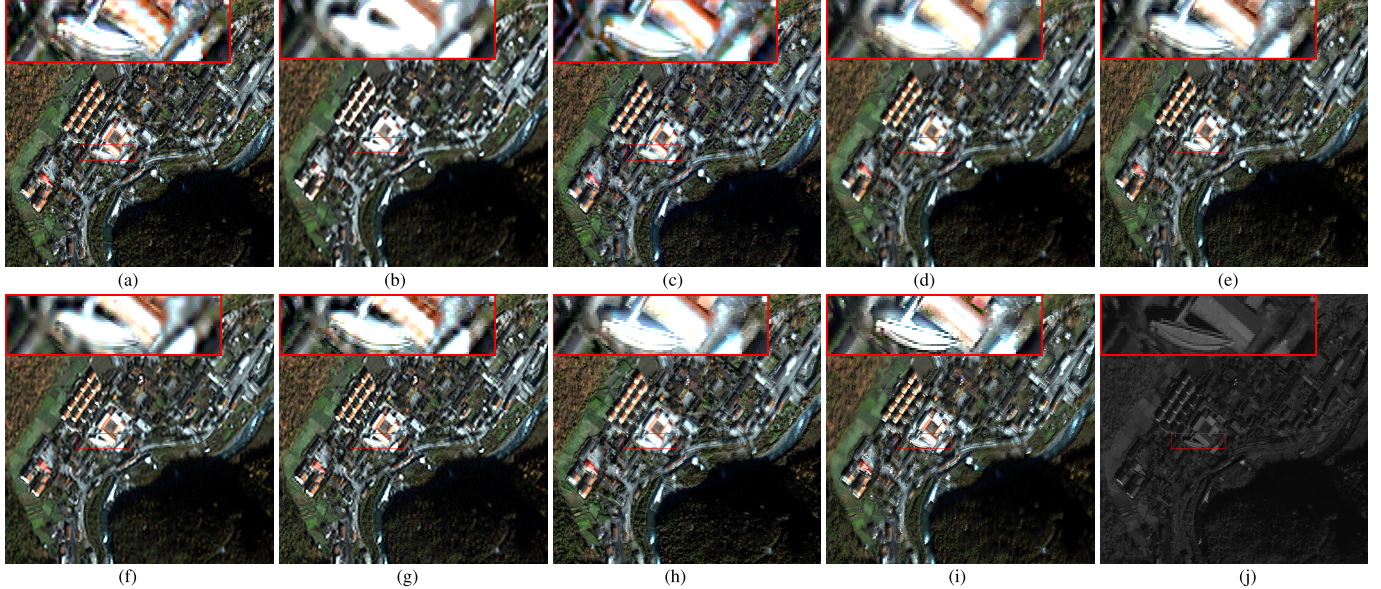


Fig. 10. Fusion results with close-ups for the compared approaches on the four-band IKONOS Sichuan dataset at full resolution (size of the PAN image: 512×576). Visual results in true colors of (a) PRACS [9], (b) RBDSD [49], (c) C-GLP [59], (d) GLP-Reg-FS [43], (e) LGC [37], (f) HQBP [60], (g) PNN [19], (h) TPNN [61], (i) proposed method, and (j) PAN image, respectively.

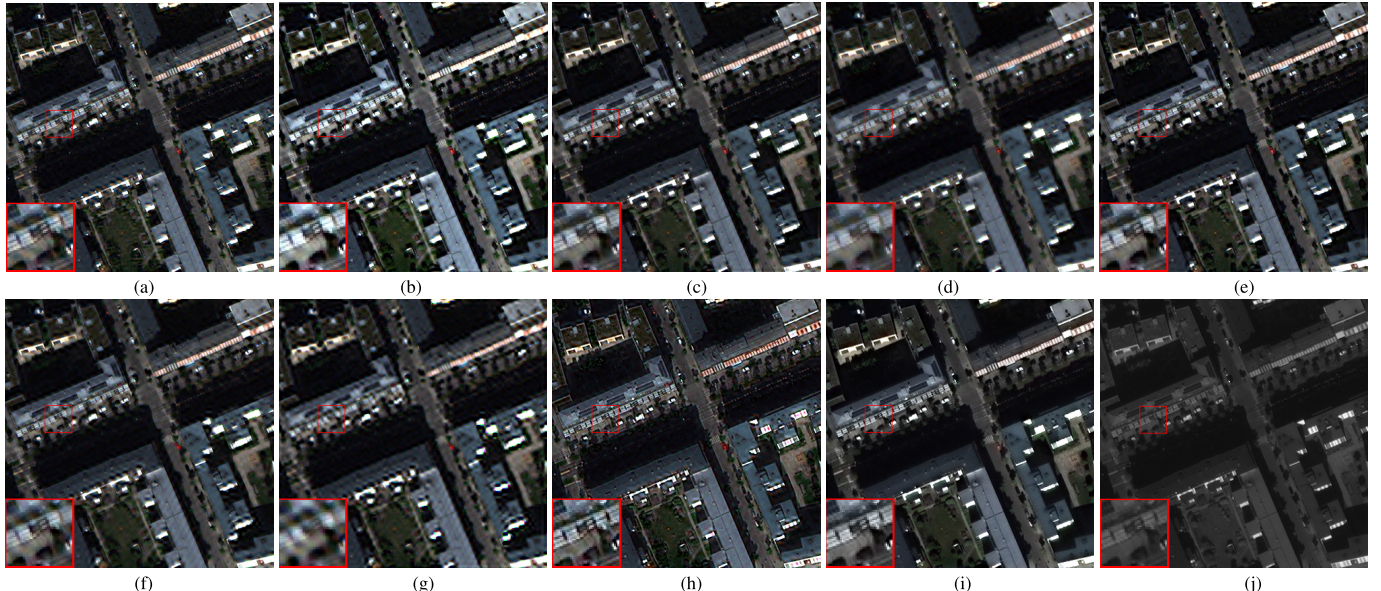


Fig. 11. Fusion results with close-ups for the compared approaches on the eight-band WorldView-2 dataset at full resolution (size of the PAN image: 256×256). Visual results in true colors of (a) PRACS [9], (b) RBDSD [49], (c) C-GLP [59], (d) GLP-Reg-FS [43], (e) LGC [37], (f) HQBP [60], (g) PNN [19], (h) TPNN [61], (i) proposed method, and (j) PAN image, respectively.

a) Submodel-I:

$$\min_{\mathbf{X}} \|\nabla \mathbf{X} - \mathbf{G} \circ \nabla \mathbf{P}\|_F^2 + \beta_1 \|\nabla_1 \mathbf{X}\|_1 + \beta_2 \|\nabla_2 \mathbf{X}\|_1 + \beta_3 \|\nabla_3 \mathbf{X}\|_1. \quad (28)$$

b) Submodel-II:

$$\min_{\mathbf{X}} \|\mathbf{XBS} - \mathbf{Y}\|_F^2 + \beta_1 \|\nabla_1 \mathbf{X}\|_1 + \beta_2 \|\nabla_2 \mathbf{X}\|_1 + \beta_3 \|\nabla_3 \mathbf{X}\|_1. \quad (29)$$

c) Submodel-III:

$$\min_{\mathbf{X}} \|\mathbf{XBS} - \mathbf{Y}\|_F^2 + \lambda \|\nabla \mathbf{X} - \mathbf{G} \circ \nabla \mathbf{P}\|_F^2. \quad (30)$$

We compared the three submodels with the proposed model on the Pléiades dataset. As shown in Table VII, all three

TABLE VII
QUANTITATIVE RESULTS FOR THE ABLATION STUDY ON THE PLÉIADES DATASET. (BOLD: BEST; UNDERLINE: SECOND BEST)

Method	PSNR	SSIM	SAM	SCC	ERGAS	Q4	Time(s)
Sub-model-I	15.53	0.192	15.730	0.831	22.351	0.208	13.35
Sub-model-II	21.20	0.519	34.867	0.655	38.372	0.596	<u>12.80</u>
Sub-model-III	<u>37.30</u>	0.966	<u>2.814</u>	<u>0.980</u>	<u>2.045</u>	<u>0.977</u>	1.911
Proposed	37.35	<u>0.965</u>	2.884	0.981	2.040	0.978	13.44
Ideal value	$+\infty$	1	0	1	0	1	-

terms are necessary to get the highest performance, and the importance of the two fidelity terms (i.e., the CDIF and the spectral fidelity term) is evident.

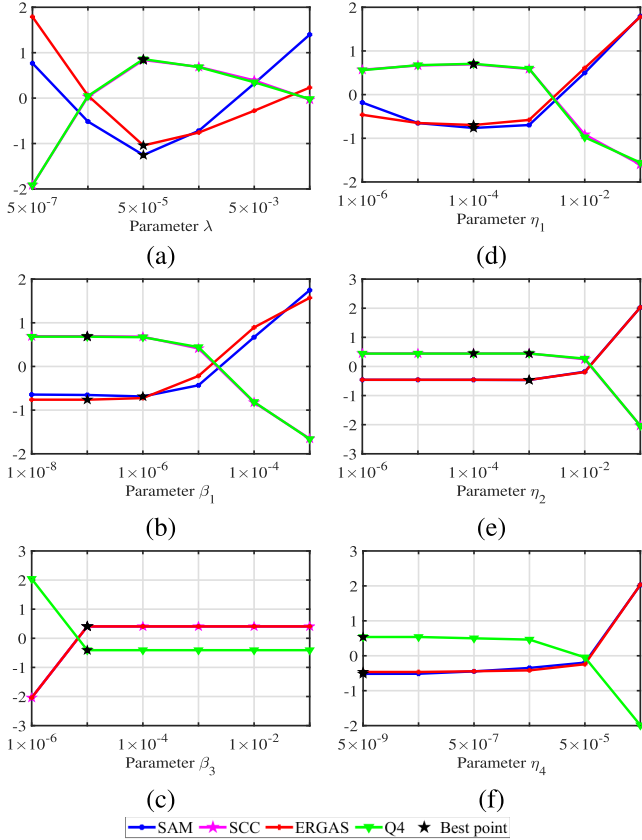


Fig. 12. Robustness analysis (using the SAM, the SCC, the ERGAS, and the Q4 as metrics) for the parameters (a) λ , (b) β_1 , (c) β_3 , (d) η_1 , (e) η_2 , and (f) η_4 on the Pléiades dataset.

TABLE VIII

QUANTITATIVE RESULTS CONSIDERING THREE DIFFERENT STRATEGIES TO ESTIMATE THE ADAPTIVE COEFFICIENTS, \mathbf{G} , ON THE PLÉIADES DATASET. (BOLD: BEST; UNDERLINE: SECOND BEST)

Method	PSNR	SSIM	SAM	SCC	ERGAS	Q4	Time(s)
Direct	20.953	0.636	10.551	0.512	12.076	0.581	<u>12.77</u>
Local	<u>34.795</u>	0.937	3.056	0.953	<u>2.580</u>	<u>0.963</u>	12.42
Proposed	37.353	0.965	2.884	0.981	2.040	0.978	13.44
Ideal value	$+\infty$	1	0	1	0	1	-

3) *Analysis About the Context-Aware Strategy:* In this article, we proposed the CDIF to extract spatial information in an effective way. Specifically, we estimated different adaptive coefficients, \mathbf{G} , for different context regions. As shown by (7), a direct way to estimate the adaptive coefficients is pixel-by-pixel. Thus, the adaptive coefficients, \mathbf{G} , can be calculated as

$$\mathbf{G} = \nabla(\mathbf{XB}) \oslash \nabla(\bar{\mathbf{PB}}) \quad (31)$$

where \oslash denotes the elementwise division. The second way is by exploiting local patches. Thus, we can split the original data in patches estimating the adaptive coefficients, \mathbf{G} , for each patch.

Thus, we compare the CDIF solution with the two other methods on the Pléiades dataset, again. The quantitative results are summarized in Table VIII. It is easy to see that the CDIF method shows the best performance.

4) *Analysis About the Number of Clusters:* The number of clusters in a context-aware strategy using a k -means clustering algorithm should be determined. Thus, we discuss, in this

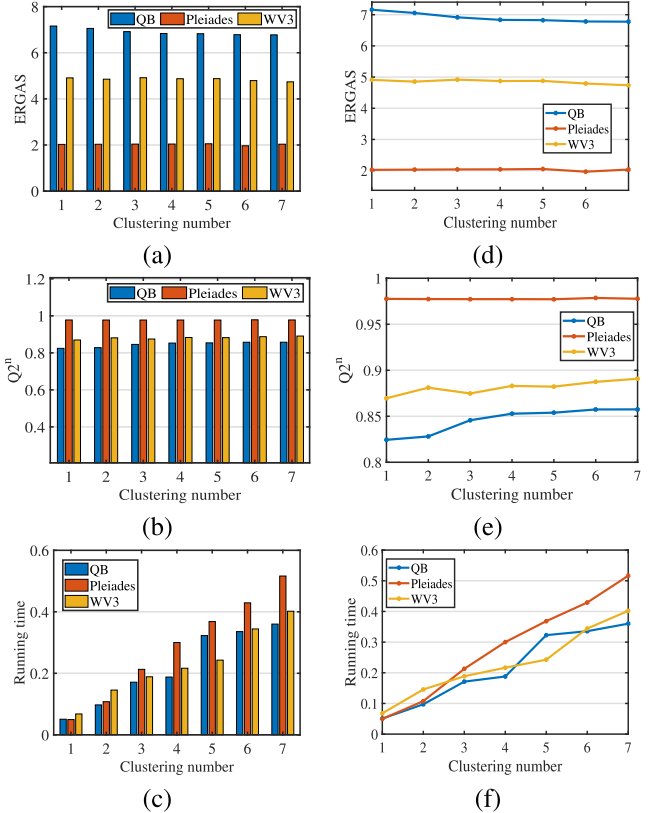


Fig. 13. Robustness analysis by changing the number of clusters. The ERGAS metric is used in (a) and (d). Instead, the Q_2^n is calculated in (b) and (e). Finally, the running times are shown in (c) and (f). WV3 and QB stand for WorldView-3 and QuickBird, respectively.

section, the influence on our approach of the changing of the number of clusters. As shown in Fig. 13, the results are quite stable by changing the number of clusters for the Pléiades test case. Instead, better results can be obtained by increasing the number of clusters for the QuickBird and WorldView-3 test cases. However, better performance is paid by an increment of the computational burden. Thus, a good balance between the fusion accuracy and the computational burden can be found by selecting a number of clusters equal to 5.

VI. CONCLUSION

In this article, we focused our attention on the CDIF with adaptive coefficients estimation. More specifically, we applied a clustering method to divide the pixels of an image into different context-based regions. Afterward, adaptive coefficients are estimated by using a regression-based method for each region. In addition, the CDIF is combined with a conventional fidelity term and a total variation regularization to formulate a novel variational pansharpening model that is solved by designing an algorithm based on the ADMM framework. The experiments conducted both at reduced resolution and full resolution demonstrated the superiority of the proposed method. Furthermore, some discussions have also been presented to the readers showing how to set the parameters of our approach, its robustness with respect to the changing of this latter, an ablation study, and the robustness with respect to the selection of a number of clusters in the proposed methodology. Future developments go toward the use of fidelity terms exploring

various domains (rather than just the gradient domain) to characterize the relationship between PAN and HRMS images. Besides, concise and effective regularizers can be developed to significantly enhance the capabilities of fidelity terms.

REFERENCES

- [1] G. Vivone *et al.*, “A new benchmark based on recent advances in multispectral pansharpening: Revisiting pansharpening with classical and emerging pansharpening methods,” *IEEE Geosci. Remote Sens. Mag.*, vol. 9, no. 1, pp. 53–81, Mar. 2021.
- [2] G. Vivone *et al.*, “A critical comparison among pansharpening algorithms,” *IEEE Trans. Geosci. Remote Sens.*, vol. 53, no. 5, pp. 2565–2586, Dec. 2015.
- [3] L. Loncan *et al.*, “Hyperspectral pansharpening: A review,” *IEEE Trans. Geosci. Remote Sens.*, vol. 3, no. 3, pp. 27–46, Sep. 2015.
- [4] H. Ghassemian, “A review of remote sensing image fusion methods,” *Inf. Fusion*, vol. 32, pp. 75–89, Nov. 2016.
- [5] A. R. Gillespie, A. B. Kahle, and R. E. Walker, “Color enhancement of highly correlated images. II. Channel ratio and ‘chromaticity’ transformation techniques,” *Remote Sens. Environ.*, vol. 22, no. 3, pp. 343–365, Aug. 1987.
- [6] P. S. Chavez and A. Y. Kwarteng, “Extracting spectral contrast in Landsat thematic Mapper image data using selective principal component analysis,” *Photogramm. Eng. Remote Sens.*, vol. 55, no. 3, pp. 339–348, Mar. 1989.
- [7] W. J. Carper, T. M. Lillesand, and R. W. Kiefer, “The use of intensity-hue-saturation transformations for merging SPOT panchromatic and multispectral image data,” *Photogramm. Eng. Remote Sens.*, vol. 56, no. 4, pp. 459–467, 1990.
- [8] C. A. Laben and B. V. Brower, “Process for enhancing the spatial resolution of multispectral imagery using pan-sharpening,” U.S. Patent 6011875, Jan. 4, 2000.
- [9] J. Choi, K. Yu, and Y. Kim, “A new adaptive component-substitution-based satellite image fusion by using partial replacement,” *IEEE Trans. Geosci. Remote Sens.*, vol. 49, no. 1, pp. 295–309, Jan. 2011.
- [10] A. Garzelli, F. Nencini, and L. Capobianco, “Optimal MMSE pan sharpening of very high resolution multispectral images,” *IEEE Trans. Geosci. Remote Sens.*, vol. 46, no. 1, pp. 228–236, Jan. 2008.
- [11] J. G. Liu, “Smoothing filter-based intensity modulation: A spectral preserve image fusion technique for improving spatial details,” *Int. J. Remote Sens.*, vol. 21, no. 18, pp. 3461–3472, Nov. 2010.
- [12] S. G. Mallat, “A theory for multiresolution signal decomposition: The wavelet representation,” *IEEE Trans. Pattern Anal. Mach. Intell.*, vol. 11, no. 7, pp. 674–693, Jul. 1989.
- [13] G. P. Nason and B. W. Silverman, “The stationary wavelet transform and some statistical applications,” in *Wavelets and Statistics*, vol. 13, A. Antoniadis and G. Oppenheim, Eds. New York, NY, USA: Springer-Verlag, 1995, pp. 281–299.
- [14] M. J. Shensa, “The discrete wavelet transform: Wedding the a trous and Mallat algorithms,” *IEEE Trans. Signal Process.*, vol. 40, no. 10, pp. 2464–2482, Oct. 2001.
- [15] G. Vivone, R. Restaino, and J. Chanussot, “A regression-based high-pass modulation pansharpening approach,” *IEEE Trans. Geosci. Remote Sens.*, vol. 56, no. 2, pp. 984–996, Feb. 2018.
- [16] Y. Yang, C. Wan, S. Huang, H. Lu, and W. Wan, “Pansharpening based on low-rank fuzzy fusion and detail supplement,” *IEEE J. Sel. Topics Appl. Earth Observ. Remote Sens.*, vol. 13, pp. 5466–5479, 2020.
- [17] Y. Yang, H. Lu, S. Huang, and W. Tu, “Pansharpening based on joint-guided detail extraction,” *IEEE J. Sel. Topics Appl. Earth Observ. Remote Sens.*, vol. 14, pp. 389–401, 2021.
- [18] W. Huang, L. Xiao, Z. Wei, H. Liu, and S. Tang, “A new pan-sharpening method with deep neural networks,” *IEEE Geosci. Remote Sens. Lett.*, vol. 12, no. 5, pp. 1037–1041, May 2015.
- [19] G. Masi, D. Cozzolino, L. Verdoliva, and G. Scarpa, “Pansharpening by convolutional neural networks,” *Remote Sens.*, vol. 8, no. 7, p. 594, Jul. 2016.
- [20] K. Zhang, W. Zuo, S. Gu, and L. Zhang, “Learning deep CNN denoiser prior for image restoration,” in *Proc. IEEE Conf. Comput. Vis. Pattern Recognit. (CVPR)*, Jul. 2017, pp. 2808–2817.
- [21] J. Yang, X. Fu, Y. Hu, Y. Huang, X. Ding, and J. Paisley, “PanNet: A deep network architecture for pan-sharpening,” in *Proc. IEEE Int. Conf. Comput. Vis. (ICCV)*, Oct. 2017, pp. 1753–1761.
- [22] L. He *et al.*, “Pansharpening via detail injection based convolutional neural networks,” *IEEE J. Sel. Topics Appl. Earth Observ. Remote Sens.*, vol. 12, no. 4, pp. 1188–1204, Apr. 2019.
- [23] H. Shen, M. Jiang, J. Li, Q. Yuan, Y. Wei, and L. Zhang, “Spatial-spectral fusion by combining deep learning and variational model,” *IEEE Trans. Geosci. Remote Sens.*, vol. 57, no. 8, pp. 6169–6181, Aug. 2019.
- [24] L.-J. Deng, G. Vivone, C. Jin, and J. Chanussot, “Detail injection-based deep convolutional neural networks for pansharpening,” *IEEE Trans. Geosci. Remote Sens.*, vol. 59, no. 8, pp. 6995–7010, Aug. 2021.
- [25] J.-F. Hu, T.-Z. Huang, L.-J. Deng, T.-X. Jiang, G. Vivone, and J. Chanussot, “Hyperspectral image super-resolution via deep spatiotemporal attention convolutional neural networks,” *IEEE Trans. Neural Netw. Learn. Syst.*, early access, Jun. 9, 2021, doi: 10.1109/TNNLS.2021.3084682.
- [26] X. Fu, W. Wang, Y. Huang, X. Ding, and J. Paisley, “Deep multiscale detail networks for multiband spectral image sharpening,” *IEEE Trans. Neural Netw. Learn. Syst.*, vol. 32, no. 5, pp. 2090–2104, May 2021.
- [27] P. Guo, P. Zhuang, and Y. Guo, “Bayesian pan-sharpening with multioriented gradient-based deep network constraints,” *IEEE J. Sel. Topics Appl. Earth Observ. Remote Sens.*, vol. 13, pp. 950–962, 2020.
- [28] X. Cao, X. Fu, C. Xu, and D. Meng, “Deep spatial-spectral global reasoning network for hyperspectral image denoising,” *IEEE Trans. Geosci. Remote Sens.*, vol. 60, pp. 1–14, 2022.
- [29] Z.-R. Jin, L.-J. Deng, T.-J. Zhang, and X.-X. Jin, “BAM: Bilateral activation mechanism for image fusion,” in *Proc. 29th ACM Int. Conf. Multimedia*, Oct. 2021, pp. 4315–4323.
- [30] Y. Wang, L.-J. Deng, T.-J. Zhang, and X. Wu, “SSconv: Explicit spectral-to-spatial convolution for pansharpening,” in *Proc. 29th ACM Int. Conf. Multimedia*, Oct. 2021, pp. 4472–4480.
- [31] D. Hong, L. Gao, J. Yao, B. Zhang, A. Plaza, and J. Chanussot, “Graph convolutional networks for hyperspectral image classification,” *IEEE Trans. Geosci. Remote Sens.*, vol. 59, no. 7, pp. 5966–5978, Jul. 2021.
- [32] D. Hong *et al.*, “SpectralFormer: Rethinking hyperspectral image classification with transformers,” *IEEE Trans. Geosci. Remote Sens.*, vol. 60, pp. 1–15, 2022.
- [33] D. Hong *et al.*, “More diverse means better: Multimodal deep learning meets remote-sensing imagery classification,” *IEEE Trans. Geosci. Remote Sens.*, vol. 59, no. 5, pp. 4340–4354, Aug. 2020.
- [34] X. Meng, H. Shen, H. Li, L. Zhang, and R. Fu, “Review of the pansharpening methods for remote sensing images based on the idea of meta-analysis: Practical discussion and challenges,” *Inf. Fusion*, vol. 46, pp. 102–113, Jun. 2018.
- [35] C. Ballester, V. Caselles, L. Igual, J. Verdera, and B. Rougé, “A variational model for P+XS image fusion,” *Int. J. Comput. Vis.*, vol. 69, no. 1, pp. 43–58, Aug. 2006.
- [36] L. Deng, G. Vivone, W. Guo, M. D. Mura, and J. Chanussot, “A variational pansharpening approach based on reproducible kernel Hilbert space and heaviside function,” *IEEE Trans. Image Process.*, vol. 27, no. 9, pp. 4330–4344, Sep. 2018.
- [37] X. Fu, Z. Lin, Y. Huang, and X. Ding, “A variational pan-sharpening with local gradient constraints,” in *Proc. IEEE/CVF Conf. Comput. Vis. Pattern Recognit. (CVPR)*, Jun. 2019, pp. 10265–10274.
- [38] P. Zhuang, Q. Liu, and X. Ding, “Pan-GGF: A probabilistic method for pan-sharpening with gradient domain guided image filtering,” *Signal Process.*, vol. 156, pp. 177–190, Mar. 2019.
- [39] L.-J. Deng, M. Feng, and X.-C. Tai, “The fusion of panchromatic and multispectral remote sensing images via tensor-based sparse modeling and hyper-Laplacian prior,” *Inf. Fusion*, vol. 52, pp. 76–89, Dec. 2019.
- [40] Y. Jiang, X. Ding, D. Zeng, Y. Huang, and J. Paisley, “Pan-sharpening with a hyper-Laplacian penalty,” in *Proc. IEEE Int. Conf. Comput. Vis. (ICCV)*, Dec. 2015, pp. 540–548.
- [41] Z.-C. Wu *et al.*, “A new variational approach based on proximal deep injection and gradient intensity similarity for spatio-spectral image fusion,” *IEEE J. Sel. Topics Appl. Earth Observ. Remote Sens.*, vol. 13, pp. 6277–6290, 2020.
- [42] S. Boyd, N. Parikh, E. Chu, B. Peleato, and J. Eckstein, “Distributed optimization and statistical learning via the alternating direction method of multipliers,” *Found. Trends Mach. Learn.*, vol. 3, no. 1, pp. 1–122, 2011.
- [43] G. Vivone, R. Restaino, and J. Chanussot, “Full scale regression-based injection coefficients for panchromatic sharpening,” *IEEE Trans. Image Process.*, vol. 27, no. 7, pp. 3418–3431, Jul. 2018.
- [44] Z.-C. Wu, T.-Z. Huang, L.-J. Deng, J.-F. Hu, and G. Vivone, “VO+Net: An adaptive approach using variational optimization and deep learning for panchromatic sharpening,” *IEEE Trans. Geosci. Remote Sens.*, vol. 60, pp. 1–16, 2022.

- [45] R. Dian, S. Li, A. Guo, and L. Fang, "Deep hyperspectral image sharpening," *IEEE Trans. Neural Netw. Learn. Syst.*, vol. 29, no. 11, pp. 5345–5355, Nov. 2018.
- [46] B. Aiazzi, L. Alparone, S. Baronti, and A. Garzelli, "Context-driven fusion of high spatial and spectral resolution images based on oversampled multiresolution analysis," *IEEE Trans. Geosci. Remote Sens.*, vol. 40, no. 10, pp. 2300–2312, Oct. 2002.
- [47] B. Aiazzi, S. Baronti, M. Selva, and L. Alparone, "Bi-cubic interpolation for shift-free pan-sharpening," *ISPRS J. Photogramm. Remote Sens.*, vol. 86, no. 6, pp. 65–76, Dec. 2013.
- [48] G. Vivone, R. Restaino, M. D. Mura, G. Licciardi, and J. Chanussot, "Contrast and error-based fusion schemes for multispectral image pansharpening," *IEEE Geosci. Remote Sens. Lett.*, vol. 11, no. 5, pp. 930–934, May 2014.
- [49] G. Vivone, "Robust band-dependent spatial-detail approaches for panchromatic sharpening," *IEEE Trans. Geosci. Remote Sens.*, vol. 57, no. 9, pp. 6421–6433, Sep. 2019.
- [50] T. Xu, T.-Z. Huang, L.-J. Deng, X.-L. Zhao, and J. Huang, "Hyper-spectral image superresolution using unidirectional total variation with tucker decomposition," *IEEE J. Sel. Topics Appl. Earth Observ. Remote Sens.*, vol. 13, pp. 4381–4398, 2020.
- [51] D. L. Donoho, "De-noising by soft-thresholding," *IEEE Trans. Inf. Theory*, vol. 41, no. 3, pp. 613–627, Mar. 1995.
- [52] Z. Wang, A. C. Bovik, H. R. Sheikh, and E. P. Simoncelli, "Image quality assessment: From error visibility to structural similarity," *IEEE Trans. Image Process.*, vol. 13, no. 4, pp. 600–612, Apr. 2004.
- [53] R. H. Yuhas, A. F. Goetz, and J. W. Boardman, "Discrimination among semi-arid landscape endmembers using the spectral angle Mapper (SAM) algorithm," in *Proc. Summaries 3rd Annu. JPL Airborne Geosci. Workshop*, vol. 1, 1992, pp. 147–149.
- [54] X. Otazu, M. Gonzalez-Audicana, O. Fors, and J. Nunez, "Introduction of sensor spectral response into image fusion methods. Application to wavelet-based methods," *IEEE Trans. Geosci. Remote Sens.*, vol. 43, no. 10, pp. 2376–2385, Oct. 2005.
- [55] L. Alparone, L. Wald, J. Chanussot, C. Thomas, P. Gamba, and L. M. Bruce, "Comparison of pancharpening algorithms: Outcome of the 2006 GRS-S data-fusion contest," *IEEE Trans. Geosci. Remote Sens.*, vol. 45, no. 10, pp. 3012–3021, Oct. 2007.
- [56] A. Garzelli and F. Nencini, "Hypercomplex quality assessment of multi/hyperspectral images," *IEEE Geosci. Remote Sens. Lett.*, vol. 6, no. 4, pp. 662–665, Oct. 2009.
- [57] L. Alparone, S. Baronti, A. Garzelli, and F. Nencini, "A global quality measurement of pan-sharpened multispectral imagery," *IEEE Geosci. Remote Sens. Lett.*, vol. 1, no. 4, pp. 313–317, Oct. 2004.
- [58] L. Alparone, B. Aiazzi, S. Baronti, A. Garzelli, F. Nencini, and M. Selva, "Multispectral and panchromatic data fusion assessment without reference," *Photogramm. Eng. Remote Sens.*, vol. 74, no. 2, pp. 193–200, Feb. 2008.
- [59] G. Vivone, S. Marano, and J. Chanussot, "Pansharpening: Context-based generalized Laplacian pyramids by robust regression," *IEEE Trans. Geosci. Remote Sens.*, vol. 58, no. 9, pp. 6152–6167, Sep. 2020.
- [60] T. Wang, F. Fang, F. Li, and G. Zhang, "High-quality Bayesian pancharpening," *IEEE Trans. Image Process.*, vol. 28, no. 1, pp. 227–239, Jan. 2019.
- [61] G. Scarpa, S. Vitale, and D. Cozzolino, "Target-adaptive CNN-based pancharpening," *IEEE Trans. Geosci. Remote Sens.*, vol. 56, no. 9, pp. 5443–5457, Sep. 2018.



Jin-Liang Xiao received the B.S. degree in mathematics from the School of Mathematics and Statistics, Yunnan University (YNU), Kunming, China, in 2019. He is currently pursuing the M.S. degree with the School of Mathematical Sciences, University of Electronic Science and Technology of China, Chengdu, China.

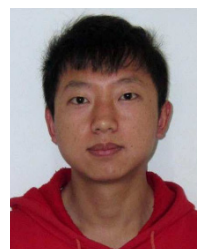
From 2016 to 2018, he was a Joint-Training B.S. Student with the School of Mathematical Sciences, Fudan University, Shanghai, China.



Ting-Zhu Huang (Member, IEEE) received the B.S., M.S., and Ph.D. degrees in computational mathematics from the Department of Mathematics, Xi'an Jiaotong University, Xi'an, China, in 1986, 1992, and 2001, respectively.

He is currently a Professor with the School of Mathematical Sciences, University of Electronic Science and Technology of China, Chengdu, China. His research interests include scientific computation and applications, numerical algorithms for image processing, numerical linear algebra, preconditioning technologies, and matrix analysis with applications.

Dr. Huang is also an Editor of *The Scientific World Journal*, *Advances in Numerical Analysis*, the *Journal of Applied Mathematics*, the *Journal of Pure and Applied Mathematics: Advances in Applied Mathematics*, and the *Journal of Electronic Science and Technology*, China.



Liang-Jian Deng (Member, IEEE) received the B.S. and Ph.D. degrees in applied mathematics from the School of Mathematical Sciences, University of Electronic Science and Technology of China (UESTC), Chengdu, China, in 2010 and 2016, respectively.

From 2013 to 2014, he was a Joint-Training Ph.D. Student with Case Western Reserve University, Cleveland, OH, USA. In 2017, he held a post-doctoral position at Hong Kong Baptist University (HKBU), Hong Kong. He also stayed at the Isaac Newton Institute for Mathematical Sciences, Cambridge, U.K., the University of Cambridge, Cambridge, and HKBU for short visits. He is currently a Professor with the School of Mathematical Sciences, UESTC. His research interests include the use of partial differential equations (PDEs), optimization modeling, deep learning to address several tasks in image processing, and computer vision, e.g., resolution enhancement and restoration.

Dr. Deng is also a member of the China Society for Industrial and Applied Mathematics (CSIAM) and the Association for Computing Machinery (ACM).



Zhong-Cheng Wu received the B.S. degree in information and computing science from the Anhui University of Finance and Economics (AUFE), Bengbu, China, in 2019. He is currently pursuing the M.S. degree with the School of Mathematical Sciences, University of Electronic Science and Technology of China, Chengdu, China.

His research interests include multispectral image fusion and spectral super-resolution.



Gemine Vivone (Senior Member, IEEE) received the B.Sc. and M.Sc. degrees (*summa cum laude*) and the Ph.D. degree in information engineering from the University of Salerno, Fisciano, Italy, in 2008, 2011, and 2014, respectively.

He is currently a Researcher with the National Research Council, Rome, Italy. His main research interests focus on statistical signal processing, detection of remotely sensed images, data fusion, and tracking algorithms.